Electric Insulation of a High-Voltage Rotating Machine for Aircraft Propulsion

Master's Thesis

Author: Víctor Barrera Consuegra

Delft University of Technology

TU Delft

Electric Insulation of a High-Voltage Rotating Machine for Aircraft Propulsion

Author: Víctor Barrera Consuegra

Student Name	Student Number
V. Barrera	5699401

Supervisors:	M. Ghaffarian Niasar, J. Dong
Teaching Assistant:	J. Wang
Project Duration:	January, 2024 - August, 2024
Faculty:	Electrical Engineering, Mathematics & Computer Science
Thesis Committee:	P. Vaessen, M. Ghaffarian Niasar, J. Dong, H. Polinder
Defense Date:	23rd August 2024

Cover: Render of E9X Elysian Aircraft, designed in collaboration with TU Delft (Modified), https://www.elysianaircraft.com/

TU Delft

Acknowledgements

This thesis project has been both fulfilling and frustrating, exponentially increasing the amount of white hairs on my head. Here I want to personally thank the people that helped me through the hard times.

First to the amazing faculty that guided me through the project and supervised my progress, Jianning Dong and Mohamad Ghaffarian Niasar. Of course to the PhD student that assisted me, to whom I hope this project is useful, Jundong Wang. Also to Farzad Nasirpour, who altruistically guided me through the laboratory going beyond his obligations.

To my friends and family waiting for me back home, who will probably never read this. To the friends I made along the way in the Netherlands, who shared my pain in this master's degree; specially to Fernando Canales who tried to help me whenever he had the chance, and to Roman Volovoy who gave advice on the writing of this project. May all of you graduate with excellent grades and invite me to your countries for a visit.

To my many roommates, with whom I shared laughs and tears during parties, exam periods, lunches and dinners, and rat hunts.

Finally to my girlfriend María Soler, who stayed by my side the whole time from 1200 km away, and never doubted me for a second. We will never have to write letters ever again.

Abstract

One fifth of the global carbon dioxide (CO_2) emissions can be attributed to the transportation sector. Consequently, the growing desire to participate in the energy transition begs for the exploration of alternative modes of transportation. This endeavor is particularly challenging in the field of aviation and aircraft propulsion, where the injection of electrification and electric motors (EMs) pose many hardships such as the need for high autonomy, light weight, high power density and reliability. This work will mainly focus on the latter.

Unlike the low voltage machines used in road mobility, the motors necessary to propel an airplane demand substantially higher voltages due to their power requirements. Despite the availability of dielectric materials and insulation techniques, an improper design of the insulation system may make it susceptible to electrical stress, possibly reaching its breakdown voltage, generating partial discharges (PDs) and degrading the insulating material overtime. This will eventually lead to the electrical failure of the machine.

This danger is further increased by the recent rise in popularity of new wide-band gap power electronic devices. These devices offer many advantages: reduced size and weight, the ability to operate in higher temperatures, and the improved efficiency due to the reduction in power losses, caused by their steep switching speed in the order of $10 - 100\,\mathrm{ns}$. However, the steep voltage transients (dv/dt) they produce create harmful side-effects to the machine. Firstly, the feeder cable connecting the voltage inverter to the machine terminals suffers Reflected Wave Phenomenon (RWP), where the voltage pulses are reflected at both ends of the line generating intereferences, which in turn generate overvoltages that can rise to up to twice the original voltage pulse. Secondly, the inherent leakage capacitance between the cable turns and the core of the stator slots produce an uneven voltage distribution along the wiring turns. These effects could increase the voltage stress in the insulator and momentarily reach the breakdown voltage in certain points of the geometry, producing Partial Discharges (PDs) that degrade the insulation over time.

To avoid this degradation, the aim of this thesis is to study these harmful effects in depth, back-up the literature review with accurate simulations and experimentation and realize the worst case scenario considering the geometry of a given motor that is currently under design. Once the phenomena is understood, some mitigation techniques are proposed to lower the chance of any discharge occurring.

Contents

Nomenclature

Abbreviations

Abbreviation	Definition
AC	Alternate Current
DC	Direct Current
CO_2	Carbon Dioxide
IEC	International Electrotechnic Commission
IEEE	Institue of Electrical and Electronics Engineers
MTL	Multi-conductor Transmission Line
PD	Partial Discharge
PWM	Pulse Width Modulation
RWP	Reflected Wave Phenomenon
RLC	Resistive, Inductive and Capacitive circuit
RC	Resistive and Capacitive circuit
VPI	Vacuum Pressure Impregnation

Symbols

Symbol	Definition	Unit
Γ	Reflection Coefficient	-
Γ_s	Reflection Coefficient at Source Side	-
Γ_L	Reflection Coefficient at Load Side	-
C	Capacitance	[F]
C_{ij}	Capacitance between Conductors i and j	[F]
C_{ig}	Capacitance to Ground of Conductor i	[F]
E	Electric Field Strength	[V/m]
I	Current	[A]
i	Instantaneous Current	[A]
j	Imaginary Unit	-
L	Inductance	[H]
L_i	Self-Inductance of Turn i	[H]
l	Cable Length	[m]

Symbol	Definition	Unit
l_c	Critical Cable Length	[m]
M_{ij}	Mutual Inductance between conductors i and j	[F]
R	Resistance	[Ω]
t	Time	[s]
t_r	Inverter Rise Time	[s]
t_p	Cable Propagation Time	[s]
u	Wave Propagation Speed	[m/s]
V	Voltage	[V]
V_{break}	Breakdown Voltage	[V]
V_+	Voltage Pulse going from Inverter to Motor	[V]
V_-	Voltage Pulse going from Motor to Inverter	[V]
v	Instantaneous Voltage	[V]
V_{dc}	DC Bus Voltage	[V]
x	Position along the line	[m]
Z	Impedance	[Ω]
Z_0	Characteristic Impedance	[Ω]
Z_L	Load Impedance	[Ω]
ω	Angular Frequency	[rad/s]

1 Introduction

In the last decades the world has seen an impressive increase in international transport through commercial flights. Consequently, the usage of jet fuel has made aviation one of the most carbon intensive activities in the transportation sector, greatly contributing to climate change. This calls for a step forward beyond the need for fossil fuels, and into more sustainable modes of transportation. This ambition has raised the interest in electric aviation, which introduces a new challenge in the field of electrical machines.

Many factors go into the design of the propulsion motors of an electrified aircraft. Besides the power rating; power density and weight, efficiency, reliability and safety are of upmost importance [1]. As newer projects arise, with bigger and more powerful airplanes, these requirements are ever increasing. In order to realize them, these designs often utilize higher voltages to improve efficiency and reduce power losses [2]. Some ongoing projects, such as the Bauhaus Luftfahrt Ce-Liner [3] and the NASA N3-X [4], work in ranges around $1 - 10\,\mathrm{kV}$ [1, 4]; substantially higher than those used in an electric car [5]. Consequentially, the high power density and efficiency requirements of a motor used in aviation, in addition to the need for a variable speed drive, make the usage of wide-band gap devices (WBGs) almost imperative; their relative light weight, temperature resistance and high switching frequency, that results in low switching losses and high efficiency, heavily outperform any other alternative [6, 7, 8].

This introduction quickly establishes the topic of PWM fed electric machines for aircraft propulsion, the general layout of the stator slots and insulation systems, and the concerns regarding their reliability and security. Two harmful side effects arise from the use of WBG devices [6, 7, 8, 9]: the Reflected Wave Phenomenon (RWP), which causes overvoltages at the motor terminals [6, 9, 10], is considered in Chapter 3; and the non-uniform voltage distribution along the machine coil turns [9, 10] is explored in Chapter 4.

The main objective of this work is gathering enough understanding of these harmful effects through literature, simulation and experimentation, and ultimately finding if these phenomena can be optimized or mitigated via any particular design choice or technique.

2

Background

This chapter focuses on the investigation done prior to the main focus of the thesis, which are explored in Chapters 3 and 4. Here, the goal is to explain the general configuration of the stator slots, the possible imperfections in the insulation, and the consequent damages to the system that may arise when it is exposed to the voltage stress caused by the RWP and the non-uniform voltage distribution. There is also a short introduction to Paschen's Law, which might increase the stresses further in machines working in conditions of low pressures, as experienced by a plane engine.

2.1. Slot Design Overview

The rotors of synchronous machines are typically subjected to relatively low electrical stresses. Even in large generators, the rotor voltage does not exceed $600\ \mathrm{V}$ [11]. Due to this, the harmful effects studied in this work do not take place in the rotor, which mainly suffers a mechanical stress through vibrations and centrifugal forces [11] and falls outside the scope of this thesis.

The focus of this section is the general configuration of the slots inside the stator. For this description it is fundamental to understand the two different wiring configurations. IEC standard defines two categories of machines based on winding insulation systems [6, 12, 13, 14]:

- Type I: machines with a DC bus voltage $\leq 700\ \mathrm{V}$ are considered to be low-voltage machines [12, 14]. These machines often utilize random-wound windings; constituted by round, insulated conductors continuously wound through the slots. Each turn in a slot could, potentially, be randomly placed next to any other turn, regardless of their voltage difference [11].
- Type II: machines with DC voltages $> 700\ \mathrm{V}$ are medium to high voltage machines. These use a more sophisticated system of form-wound windings and insulation. In this case, the turns of the copper conductor are placed in an organized manner, usually on top of each other. This ensures that voltage difference will be minimized between neighboring turns [11].

Considering the voltages present in the motor, the use of a form-wound stator is advisable, as it is also recommended in [11] for voltages above $> 1\ \mathrm{V}$.

The slot of a form-wound stator is generally a rectangular (or similarly shaped) chamber, carved along the whole length of the inside of the stator. The top of the chamber is open to allow the encasing of the wiring and insulation systems, and is later closed off using a non-conductive and non-magnetic wedge to prevent the loosen of its contents, which might lead to abrasion of the materials. The stator core is usually made of iron or magnetic steel to concentrate the magnetic field, and is connected to ground [11, 15], thus the inside walls of the stator are also known as groundwalls.

The copper conductor, usually with a flattened rectangular shape and bent into a diamond-like coil [14] (see Figure 2.1a), with each subsequent turn next to or on top of one another. Of course, a single slot does not contain the whole coil, but only half of it. Therefore, there is an area outside of the slot where the coil emerges to enter another slot: this is know as the overhang area [15], which is observable in the motor in Figure 2.1b, built by Schulz Electric [16]. Prior to the insertion inside the slots, the coils are insulated and preformed into the desired shape. In order to prevent losses to the Skin Effect (discussed in Subsection 4.1.3), the copper conductor if often divided into several smaller conductors -or strands- separated by a thin insulating resin called strand insulation.

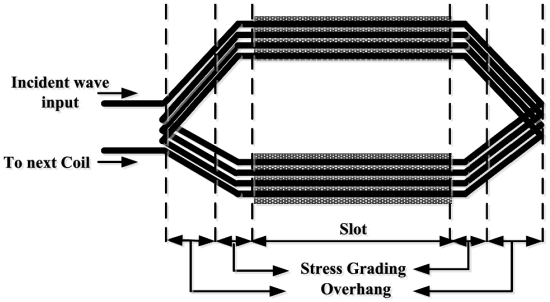

(a) Schematic of a form-wound coil [17].

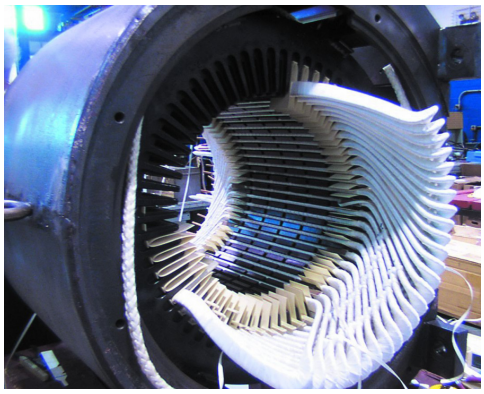

(b) Motor stator build by Schulz Group [16]. The overhang area clearly visible.

Figure 2.1: Depiction of a form-wound stator coil (left) and a real-life demonstration (right).

The insulation system consists of three main components [6]. First, the strand insulation is an enamel or resin that coats all the copper strands within a single wire. Due to the low voltage difference between them, this coating can be particularly thin without implying any risk. Secondly, the turn insulation is a coating covering the whole cable itself, which galvanically separates each coil turn from each other, preventing a short-circuit between them that could overheat the system and cause damage to the machine [11], [18]. The strand insulation and the turn insulation are sometimes combined using the same material, although in such cases an extra enamel sleeve is applied to improve it. Lastly, the groundwall insulation prevents shorts between the medium voltage wiring and the grounded slot walls of the stator. This is typically the thickest element, and is made of derivatives of mica (mica tape or a mixture of mica flakes in epoxy resin) which is a great dielectric material and resistant to corona discharges [11, 18]. The whole slot configuration with its components is depicted in Figure 2.2.

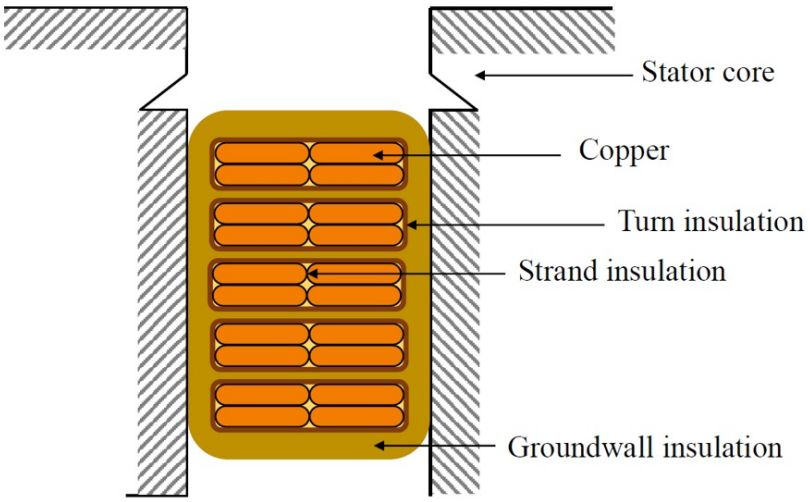

Figure 2.2: General slot configuration of a form-wound stator [6].

2.2. Partial Discharges

According to IEEE Dictionary (IEEE Standard 100-1996 [19]), the term Partial Discharge (PD) refers to a category of electric discharges that do not completely bridge the gap between two conductors, involving instead only a portion of the dielectric material insulating them [20]. This section explains the reason for their appearance in the slot insulation and the problems they entail.

2.2.1. Air Pockets in Insulation

The state-the-art materials used in electric machine insulation systems have proven time and time again to be exceptionally effective. Enamels and resins such as epoxy resin are popular for strand and turn insulation for their great mechanical and thermal properties, while mica flake tapes are typically used in higher voltage machine, and specially in groundwall insulation due to their high dielectric strength, thermal endurance and resistance to corona discharges [15, 18]. Even high voltage stator windings, with a design electric stress of up to $3\ \mathrm{kV/mm}$ RMS during operation, are sufficiently insulated using mica tape. In fact, those stresses are about 100 times lower than the capabilities of modern mica-based insulation agents [11], partly justifying their undisputed dominance over other systems.

However, during the process of manufacture, the insulation system is prone to develop defects such as micro-cavities or small air bubbles, usually due to faulty adhesion between the tapes or simply imperfection in the material [6, 11]. Since the breakdown voltage of air is many times lower than that of the typical solid insulators ($\sim 9\ \mathrm{kV/mm}$ at $100\mathrm{kPa}$) [11], partial discharges are bound to take place inside these air bubbles (see Subsection 2.2.2), causing sparks that can damage the insulator and grow the air pocket in size overtime. This will eventually lead to a total failure of the insulation system [6, 11, 18]. Moreover, according to Paschen's Law the breakdown voltage of air can decrease further depending on the atmospheric pressure (see Subsection 2.2.3) [21, 22, 23].

Many techniques have been developed to minimize or prevent air pockets from forming: slot pressing is done to squeeze the air out of the cavities [18]; Vacuum Pressure Impregnation (VPI) is often used as an effort to fill the pockets with epoxy resin; and a semiconductive, low-resistance silicon carbide coating is sometimes applied to the slot walls in order to dilute the electric stress on the groundwall insulation [11]. Nonetheless, none of these techniques have proven to eliminate the appearance of PDs, and therefore this thesis studies alternatives to reduce the electric stress applied to the system.

2.2.2. Partial Discharges in Air Pockets

Under standard conditions of pressure and temperature, and relatively low electric fields, gases such as air are reasonably good insulators. On the contrary, when exposed to higher electric fields some molecules can gain sufficient kinetic energy to ionize upon impact with other particles. Thought processes beyond the scope of this work (explained in *High Voltage Engineering Fundamentals* [23]), this cascades into a macroscopic ionization of air in a small region inside the cavity, causing a spark known as partial discharge. In simple terms, PDs are bound to occur whenever the electric field in the region exceeds the breakdown electric field $E > E_{breakdown}$. As previously discussed, the breakdown field of most gases is significantly lower than that of the insulator ($\sim 3\ \mathrm{kV/mm}$ at $100\ \mathrm{kPa}$ in H_2 gas, and $> 300\ \mathrm{kV/mm}$ for usual insulating materials [11]).

To further understand the cause of these PDs, consider the cross-section of an insulated stator slot as shown in Figure 2.3. Considering the galvanic isolation between the conductors and stator and their voltage difference, there is a capacitive relation between the two. As such, an electric equivalent circuit can be drawn in Figure 2.4, where the total voltage difference can be separated into voltage drops for across both capacitors C_{air} and C_{ins}, representing the cavity and the groundwall insulator respectively.

Hence, the voltage drop across the capacitor corresponding to the air bubble C_{air} can be easily found through circuit theory and is described by Eq. 2.1.

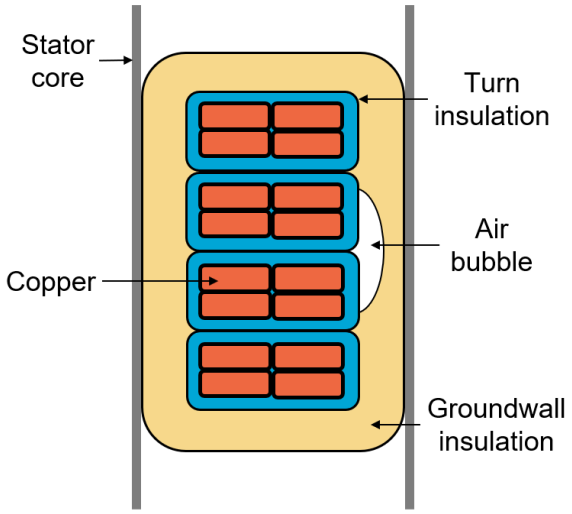

Figure 2.3: Cross-section of a form-wound stator slot with an air cavity in the groundwall insulation. Based on a drawing by Greg C. Stone [11].

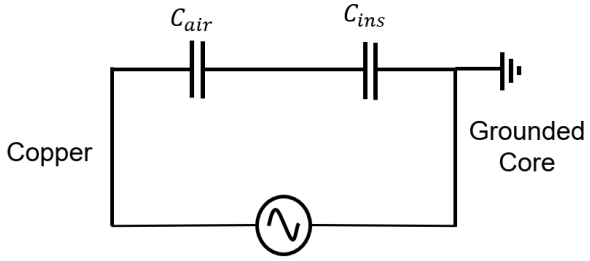

Figure 2.4: Equivalent circuit of the slot cross-section, showcasing the stresses in the air bubble and the insulator.

$$V_{air} = \frac{C_{ins}}{C_{air} + C_{ins}} V_{total} \tag{2.1}$$

By considering, for instance, that the air pocket size is 5% of the total insulation system, the capacitances C_{ins} and C_{air} can be calculated to a first approximation as a parallel plate capacitor:

$$C_{air} = \frac{\epsilon_0 \, A}{0.05 \, d} \tag{2.2}$$

$$C_{ins} = \frac{\epsilon_0 \, \epsilon_r \, A}{0.95 \, d} \tag{2.3}$$

Assuming the insulation is based on a mica tape with relative permittivity around $\epsilon_r = 6$, the voltage drop through the air bubble is calculated with Eq. 2.1:

$$V_{air} \approx 0.24 \, V_{total} < V_{break} \tag{2.4}$$

Unfortunately, at such sizes it is not accurate to calculate the breakdown voltage linearly. Instead, the correct value can be found using the Paschen's curve, which is far more adequate at such distances. An example is showcased in Subsection 2.2.3.

$$V_{break} = \int_{pocket} \vec{E}_{break} \, \vec{dx} \neq E_{break} \, x \tag{2.5}$$

2.2.3. Paschen's Law

It has been experimentally established since 1889 by Friedrich Paschen that the electric breakdown voltage of a gas is strongly influenced by its pressure and humidity [11, 23, 24, 25]. This dependence is not linear and can pose a serious concern for the design of an electrical machine used in aviation. Due to the great heights in which they operate, the pressure descent can modify the breakdown voltage according to Paschen's Law [24]:

$$V_{break} = \frac{B\ p\ d}{\ln(p\ d) + k} \tag{2.6}$$

Where k is:

$$k = \ln\left(\frac{A}{\ln(1 + \frac{1}{\gamma})}\right) \tag{2.7}$$

Where p is the gas pressure and d is the distance between electrodes in an air filled capacitor. The parameters A, B and γ are constants dependent on the characteristics of the gas. In this context, the breakdown voltage depends on the pressure of the gas that fills the air pocket, and the size of said pocket. Figure 2.5 displays the relation between breakdown voltage and the product of pressure and distance pd, known as Paschen's curve. It is interesting to notice that the graph presents a clear minimum at a value close to $800\ \mathrm{Pa\ m}$

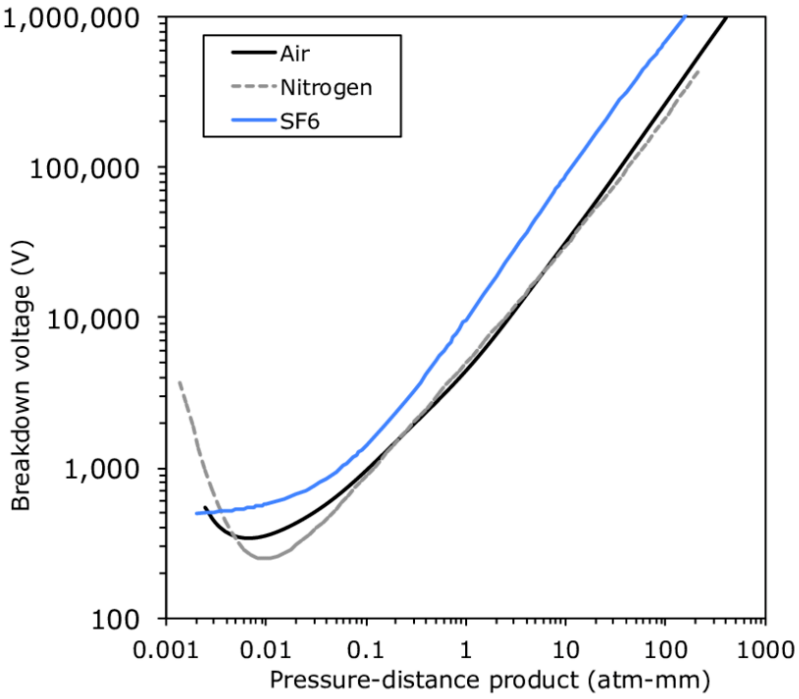

Figure 2.5: Paschen curves for some gases. [26]

At the typical altitudes of commercial air travel (assume around $10000\ \mathrm{m}$), the air pressure is close to $0.2\ \mathrm{atm}$. In this example let's consider an insulation thickness of $d = 1\ \mathrm{mm}$, very common among cable manufacturers. By computing the same case assumed in Subsection 2.2.2, with an air bubble of 5% the thickness of the insulation, the breakdown voltage can be inferred from the graph in Figure 2.2.3 to be around $V_{break} = 350\ \mathrm{V}$. Therefore, by virtue of Eq. 2.4, the maximum voltage across the insulation in these conditions would be:

$$V_{total} < \frac{V_{break}}{0.24} = 1458.3 \text{ V} \tag{2.8}$$

While this law goes beyond the scope of this project, it is encouraged to investigate further into the theory behind it and find appropriate parameters for air to use in Eq. 2.6, as it is vital for the design of a durable stator slot insulation. Note that the calculations from Eq. 2.2, Eq. 2.3 and Eq. 2.8 are made with many assumptions based on the typical thickness of plastic insulation of cable manufacturers.

3

Reflected Wave Phenomenon (RWP)

This chapter focuses in the investigation of the Reflected Wave Phenomenon RWP. Section 3.1 is a deep exploration of the literature covering this issue, with the goal of understanding and mitigating its harmful effects. Secondly, Section 3.2 is an explanation of the methodology used in this project to test the veracity of previous articles and adapt it to the current system. Lastly, the results are presented and contrasted with previous studies in Section 3.3to draw conclusion on the best practice for mitigation.

3.1. Literature Review

During the mid 20th century, one of the first few documented occurrences of RWP was observed in a section of the Southern Region of British Railways cable network. The installation between Croydon and Three Bridges operated successfully from 1932 to 1944, when an incidence rise of $33\ \mathrm{kV}$ cable failures prompted S.B.Warder to publish a study [27]. In his research he concluded that these failures were cause by harmonics generated in the rectifier equipment. For some time, it was generally believed that this effect would only take place in fairly long cables ($> 30\ \mathrm{m}$) [28], and therefore smaller projects would remain safe from the harmful effects.

Later down the line, as semiconductor technology progressed, it became apparent that smaller machines were not immune to the overvoltages produced by the inverters. In the late 1980s some authors like Peter G. McLaren [29] and Erik Persson [30] started relating this effect to the faster rise times of the semiconductor devices used in electric motor drives. Nowadays, the steep fronts of PWM voltage surges (dV/dt) are widely known to be partly responsible for the premature failure of low and medium-high voltage machines [6, 7, 8, 10, 28, 31].

The objective of this literature review is to gain a deep insight in the current understanding of the RWP, and explore the state-of-the-art technology and technique for the mitigation of this effect or its harmful consequences. This phenomenon can be approached from two perspectives: the time domain and the frequency domain. For the sake of simplicity, this work focuses in the time domain study of the RWP. For a better comprehension of the frequency domain study, this author suggests these resources: [32, 33, 34, 35].

3.1.1. Transmission Line Theory

As a result of the distributed leakage capacitances and inductances, and the high frequency of the PWM pulses, the feeder cable between the inverter and the motor terminals behaves as a transmission line [8, 31, 36, 37]. As such, the RWP should be understood using Transmission Line Theory. A simple

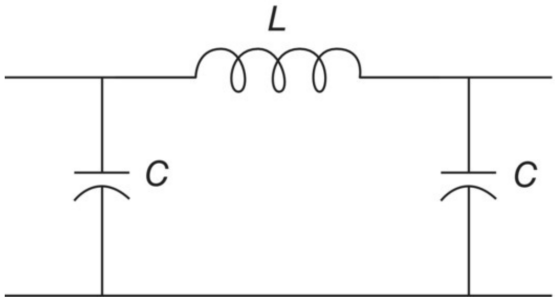

Figure 3.1: PI-section model of a lossless transmission line, *Electric Power Principles*, Chapter 3, [38].

example of a transmission line model is seen in Figure 3.1, showcasing the intrinsic capacitance and inductance of a lossless cable as a lumped parameter 'PI-section' model.

Therefore, the transmission line behaviour of the feeder cable is described by the Telegrapher Equations (Eqs. 3.1 & 3.2). Ultimately, all parameters and formulas that describe this phenomenon are derived from solving these differential equations. The following derivation is based on the 3rd chapter of *Electric Power Principles*, by James L. Kirtley [38].

$$\frac{\partial v}{\partial x} = -L\frac{\partial i}{\partial t} \tag{3.1}$$

$$\frac{\partial i}{\partial x} = -C\frac{\partial v}{\partial t} \tag{3.2}$$

These equations describe the voltage and current distributions along the transmission line length x when subjected to a change in voltage or current in the time domain. L and C are the inductance (H/m) and capacitance (F/m) per unit length of the cable. By applying a cross-differentiation to both equations, the result is as follows:

$$\frac{\partial^2 v}{\partial x^2} = -L\frac{\partial^2 i}{\partial x \partial t} \tag{3.3}$$

$$\frac{\partial^2 i}{\partial x^2} = -C\frac{\partial^2 v}{\partial x \partial t} \tag{3.4}$$

By substituting the original Telegrapher Equation 3.2 into Eq. 3.3, a voltage wave equation is obtained 3.5. Note that a similar process can be applied to Eq. 3.4 for a current wave equation, omitted to avoid redundancy.

$$\frac{\partial^2 v}{\partial x^2} = LC\frac{\partial^2 v}{\partial t^2} \tag{3.5}$$

By definition, the propagation speed u of the wave is defined as $u = 1/\sqrt{LC}$. Moreover, by virtue of wave equation it is known that their general solutions have the following form:

$$v(x,t) = v_+(x-ut) + v_-(x+ut) \tag{3.6}$$

$$i(x,t) = i_+(x-ut) + i_-(x+ut) \tag{3.7}$$

Where the terms v_+ and v_- are particular solutions of the differential equation. In this particular context, v_+ is a wave or pulse travelling 'forward' (from the inverter to the motor terminals), while v_- is a 'backward' travelling pulse (from motor terminals to inverter).

Characteristic Impedance

The characteristic impedance of the line is defined through a short derivation starting from differentiating Eq. 3.7, and then substituting the original Telegrapher Equation 3.1, yielding:

$$\frac{\partial i}{\partial t} = \mp u \frac{\partial i}{\partial x} \tag{3.8}$$

$$\frac{\partial v}{\partial x} = \pm uL \frac{\partial i}{\partial x} \tag{3.9}$$

Then by integrating with respect to x it results in:

$$v_{\pm} = \pm uLi_{\pm} \tag{3.10}$$

From Ohm's Law it is known that the voltage and current are related through the impedance. In addition, the previous definition of propagation speed in the line is useful to define its characteristic impedance Z_0 as follows:

$$uL = \frac{L}{\sqrt{LC}} = \sqrt{\frac{L}{C}} = Z_0 \tag{3.11}$$

With such definition and the relation established in Eq. 3.10, the general solutions of the Telegrapher Equations describe the transmission line excitation as:

$$v(x,t) = v_+(x - ut) + v_-(x + ut) \tag{3.12}$$

$$i(x,t) = \frac{1}{Z_0}(v_+(x - ut) - v_-(x + ut)) \tag{3.13}$$

Reflection Coefficient

At the end of the feeder cable the transmission encounters a separate impedance correspondent to the motor, the load impedance Z_L. At this point Ohm's Law may be applied again to find the ratio between voltage and current:

$$\frac{v_+ + v_-}{i_+ + i_-} = Z_L \tag{3.14}$$

Considering the previous expression of the line current in Eq. 3.13, the following substitution can be made:

$$\frac{v_+ + v_-}{v_+ - v_-} = \frac{Z_L}{Z_0} \tag{3.15}$$

Finally, by reorganizing the terms it is trivial to find the relationship between the incoming forward wave v_+ and the backward wave v_-:

$$v_- = v_+ \frac{Z_L - Z_0}{Z_L + Z_0} \tag{3.16}$$

Hence defining the Reflection Coefficient Γ_L (Eq. 3.17). This parameter describes a reflection at the motor terminals, when the incoming v_+ experiences a mismatch in impedance of its medium of travel.

Upon reflection, the backwards travelling pulse v_- is emitted from the terminals, resulting in wave interference with the forwards pulse v_+, giving the final value of $v(x_L, t) = v_+(x_L, t) + v_-(x_L, t)$.

$$\Gamma_L = \frac{Z_L - Z_0}{Z_L + Z_0} \tag{3.17}$$

In light of the aforementioned coefficient, it is interesting to consider the various particular cases that can arise from the different possible mismatches in this system:

- Load impedance equal to characteristic impedance ($Z_L = Z_0$). There is no reflection since $\Gamma = 0$.
- *Open* line ($Z_L \to \infty$). The reflection is of the same sign as the incoming pulse, and has the same magnitude since $\Gamma = 1$.
- *Shorted* line ($Z_L = 0$). The reflection has the same magnitude but opposite sign given $\Gamma = -1$

Note that in the case on an 'Open line', the resulting terminal voltage will be approximately double that of the DC bus voltage according to $v(x_L, t) = 2\, v_+(x_L, t)$. It is also relevant to mention that this analysis is done assuming an ideal lossless transmission line.

3.1.2. Bewley Diagram

As mentioned before, the voltage reflections occur at regions with an impedance mismatch. Therefore, there will be none throughout the whole span of the feeder cable given its relatively constant parameters along its length. There are two impedance mismatches, however, at both ends of the line: at the inverter and at the motor terminals.

In general, the inductive nature of electric machines makes the load impedance much greater than the characteristic impedance of the cable, usually 10 to 100 times higher [36], resulting in a reflection coefficient close to one $\Gamma_L \approx 0.9$ in smaller machines [39]. In this scenario, the magnitude of the reflected backwards pulse will be close to that of the incoming forwards pulse, creating the overvoltage and almost doubling the DC bus voltage. As a rule of thumb, the reflection coefficient and, thus, the overvoltage magnitude decrease with power rating according to [8, 28].

On the other hand, at the inverter side the DC bus capacitance will behave as a short circuit where $Z_s = 0$ [39]. In this case, following Eq. 3.17 the reflection coefficient at the source will be negative $\Gamma_s = -1$. This results in an almost perfect reflection with and opposite sign, sending an inverted forward pulse back to the motor. As a consequence the wave interference at the inverter is destructive, leaving the source voltage at the constant DC voltage V_{dc}. In order to properly follow the subsequent interferences between the forward and backward pulses, the literature suggests the use of a Bewley lattice diagram (see Figure 3.2).

In Subsection 3.1.1 the propagation speed u of the transmission line was defined. The propagation time t_p is subsequently defined as the time the pulse takes to travel from one end of the line to the other, and given the finite propagation speed u and cable length l, it is non-zero. In the diagram, the voltages V_{Li}^- and V_{si}^- refer to the same pulse V_i^-, at the load side and source side respectively.

$$t_p = \frac{l}{u} \tag{3.18}$$

First, the inverter sends a pulse with a certain voltage step $0 \to V_{dc}$ and a certain rise time t_r. During the first propagation period $0 \to t_p$ nothing happens at the motor side, as the pulse has still not reached the line termination. Once the wave hits the terminal at t_p (***point 1*** in Figure 3.2), the first backward reflection V_1^- occurs, interfering with the initial pulse and increasing the voltage to $(1 + \Gamma_L)V_{dc}$ in a time-frame of t_r. After that, the reflected V_1^- travels back to the inverter and gets reflected again after another period $t_p \to 2t_p$ creating the second forward pulse V_2^+. Notice that at the inverter $V_{s1}^- + V_{s2}^+ = 0$,

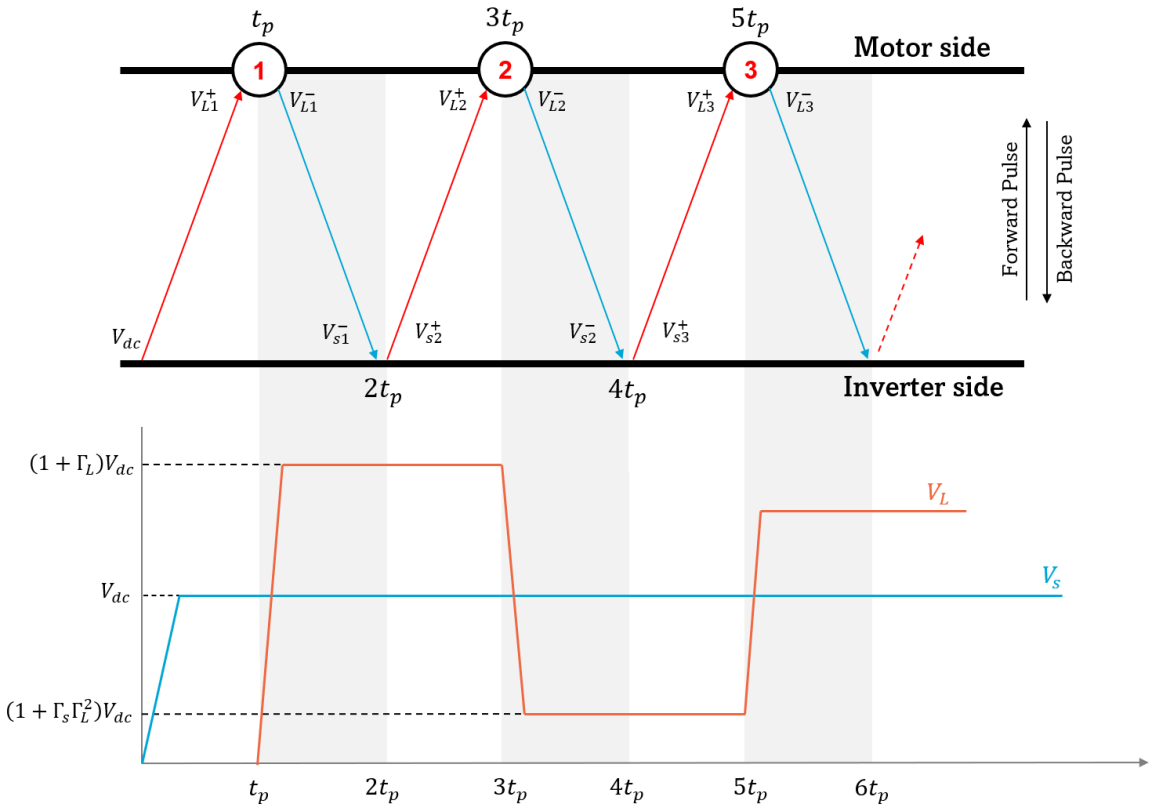

Figure 3.2: Bewley lattice diagram (up) and the corresponding source and load voltages (down). Based on Phd thesis from Wenzhi Zhou, University of Bristol [8].

since $\Gamma_s = -1$, thus the voltage remains constant at V_{dc}. This second forward pulse travel back to the motor $2t_p \rightarrow 3t_p$ and hits it at *point 2*, two propagation times later than *point 1*. The negative sign of V_2^+ causes the resulting overvoltage wave to go down to $(1+\Gamma_s\Gamma_L^2)V_{dc}$ [31, 32]. This process repeats again after two propagation periods $3t_p \rightarrow 5t_p$, completing the whole *resonance period* [8] of the overvoltage wave, with an oscillation frequency of:

$$f_{rwp} = \frac{1}{4t_p} \tag{3.19}$$

3.1.3. Rise Time and Critical Length

As previously stated, in the late 1980s author such as Peter G. McLaren [29] and Erik Persson [30] established a connection between the overvoltage caused by the RWP, the rise time of the switching devices in the motor drives, and the length of the feeder cable connecting the inverter to the motor. In essence, the relationship involves the rise time t_r of the inverter switches and the pulse propagation time t_p of the cable, from Eq. 3.18. For a fixed length l, thus fixed propagation time t_p, slower rise times t_r result in smaller overvoltages, since the pulse does not have time to grow to its maximum value before the next reflection dampens it. On the other hand, faster t_r allow the pulse to reach its maximum. The same analysis is also valid by fixing t_r, longer cables are prone to higher overvoltages while shorter ones allow the dampening by following reflections.

The maximum value of the overvoltage spike is limited by the Transmission Line Theory at $(\Gamma_L + 1)V_{dc}$. Therefore, considering a fixed rise time t_r, the critical length l_c is defined as the minimum cable length that permits the maximum voltage growth [6, 32, 39, 40].

Annette von Jouanne [36] proposed a quick analysis where the negative reflection V_2^+ (see Figure 3.2) hits the motor terminals after 3 travels through the transmission line, at $3t_p$, so the rise time must be faster than that to achieve the maximum peak value. The suggested formula, cited by some other authors [32, 36, 37, 40], defines the peak voltage for faster and slower values:

$$V_{peak} = \begin{cases} V_{dc} + \Gamma_L V_{dc} & \text{if } t_r \leq 3t_p \\ \frac{3l_c V_{dc} \Gamma_L}{v t_r} + Vdc & \text{if } t_r > 3t_p \end{cases} \tag{3.20}$$

Notice that the threshold in between maximum overvoltage and lower values is fixed by comparison between t_r and t_p. The critical length is hence defined by:

$$l_c = \frac{ut_r}{3} = \frac{t_r}{3\sqrt{LC}} \tag{3.21}$$

However, it is fundamental to remember that during the first propagation time $0 \rightarrow t_p$ the motor terminal is still not involved in the phenomenon, since the pulse is yet to reach it. After t_p, the first reflection only takes two more propagation times to go to the inverter, change its sign and come back to the motor. Consequently, other authors like Robert W. Maier [41] suggest Eq. 3.22 instead:

$$V_{peak} = \begin{cases} V_{dc} + \Gamma_L V_{dc} & \text{if } t_r \leq 2t_p \\ \frac{2l_c V_{dc} \Gamma_L}{v t_r} + Vdc & \text{if } t_r > 2t_p \end{cases} \tag{3.22}$$

Where the critical length would be that which makes the rise time equal these two propagation times [6, 41]:

$$l_c = \frac{ut_r}{2} = \frac{t_r}{2\sqrt{LC}} \tag{3.23}$$

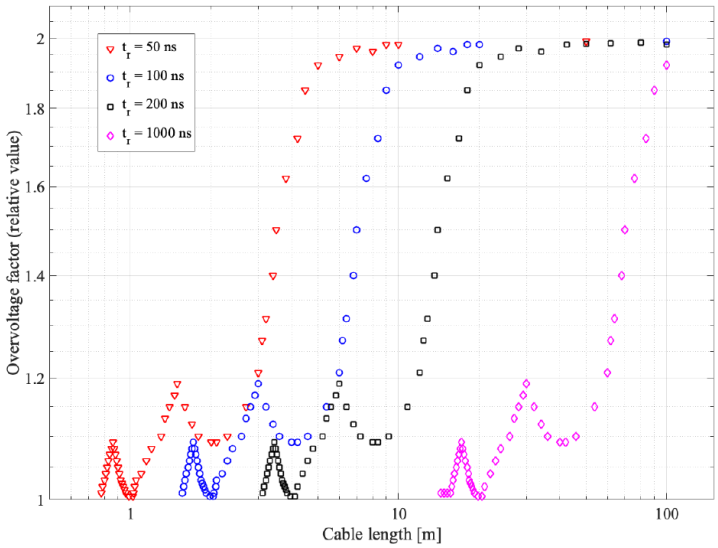

Figure 3.3: Dependence of overvoltage peak value over cable length, for various inverter rise times. Based on a study by Jeremy C. G. Wheeler [6, 42].

While the latter analysis is more aligned with the terminal voltage explored in the Bewley lattice diagram, both formulas claim that for shorter cable lengths the peak voltage shows a linear decrease with length. Therefore, the optimal situation would present either an infinitely short feeder cable, or alternatively an infinitely long rise time. However, some authors conducted a study of this threshold through simulation and/or experimentation [6, 8, 32, 42] which disprove the formulas presented by von Jouanne and Maier

in Figure 3.3. In these studies, the peak overvoltage shows a much faster linear descent on decreasing cable lengths, followed by several spikes of lower magnitude.

Considering the lack of consensus between these articles, this section focuses on recreating the study by building a model in MATLAB Simulink and analysing the results with the aid of the Bewley lattice diagram.

3.2. Model & Methodology

In order to test the hypothesis established by the literature in Eq. 3.20 and 3.22, a Simulink model is built following the simple schematic presented in [10]. The model consists of a step voltage source with controllable rise time t_r, a distributed parameter transmission line with per unit impedance, resistance and leakage capacitance, and a simplified load representing the motor (see Figure 3.4). For the sake of simplicity and comprehension of this phenomenon, the motor impedance Z_L is considered purely resistive. Although this consideration is far from reality, it will have a small effect in the rise time-cable length analysis in light of Eq. 3.17.

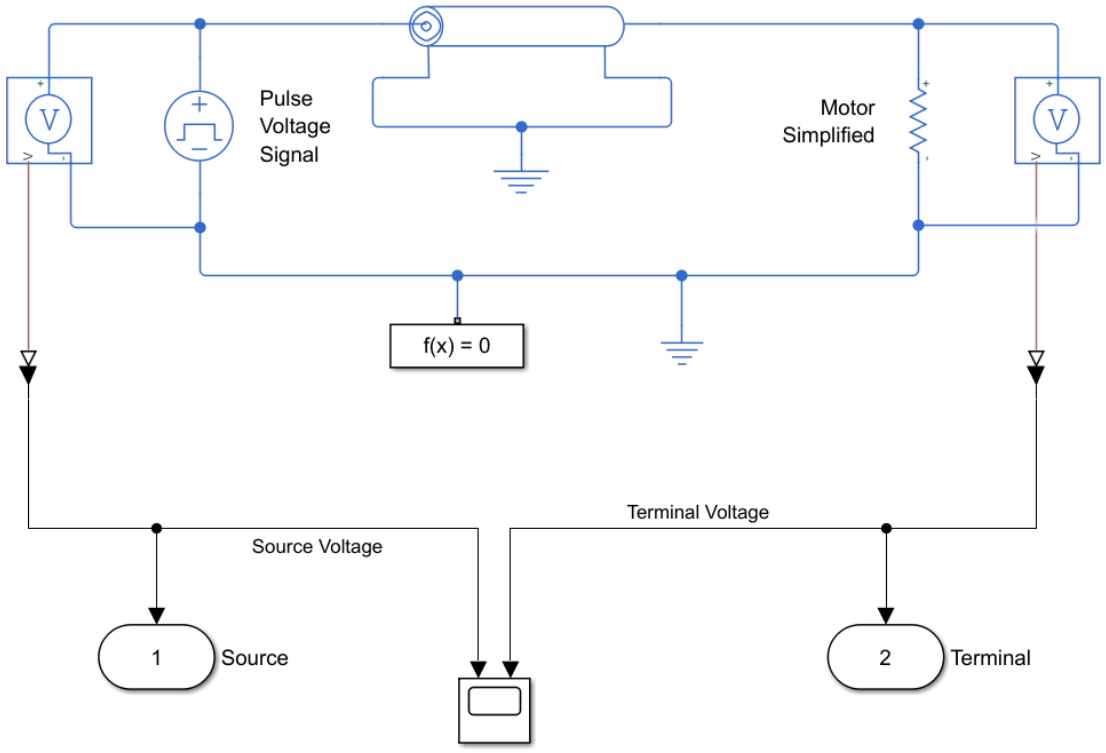

Figure 3.4: Simscape Simulink model of the 1-phase feeder cable and motor.

After source and load are connected through the transmission line, the circuit is closed and grounded as an electric reference to measure voltages. Both components are the end points of the cable have their voltage waveform measured and plotted into a scope, as well as sent through output blocks to a MATLAB script for post processing. The parameters of each component, shown in Table 3.4, are rough estimates based on literature [6, 28, 36, 37, 40] and are meant to amplify the effect of RWP as much as possible to discern any nuances of the circuit response.

The formula proposed by von Jouanne [36] in Eq. 3.20 was admittedly representing a peak line-to-line voltage in a 3-phase machine. As a precautionary measure, a more complex 3-phase model is also

Magnitude	Value	Units
Cable Resistance	1	$\mathrm{m\Omega/m}$
Cable Inductance	1	$\mu\mathrm{H/m}$
Cable Capacitance	500	$\mathrm{pF/m}$
Cable Z_0	~ 44.72	Ω
Motor Impedance Z_L	3000	Ω
Reflection Coefficient	~ 0.97	$-$
Source Voltage step V_{dc}	200	V

Table 3.1: Electrical parameters of the 1-phase model from Figure 3.4

.

built to ensure the results will not differ when considering a real-life motor (Figure 3.5). Considering the switching pattern of a 3-phase H-Bridge converter [43, 44] the instantaneous L-L voltage at the moment of a single switch transition can either be 0 or $\pm V_{dc}$. As such, the simulation includes 3 transmission lines with 3 loads fed by 3 pulse source blocks, which pattern consists of 2 phases at constant voltage $V_b = V_{dc}$ and $V_c = 0$, while one of them switches $V_a = 0 \rightarrow V_{dc}$. This time, the motor is Y-connected with a floating neutral point. The expected result is roughly the same as the single phased model, but the possibility of interactions between phases through the neutral point is not discarded, which could explain the discrepancies in the literature.

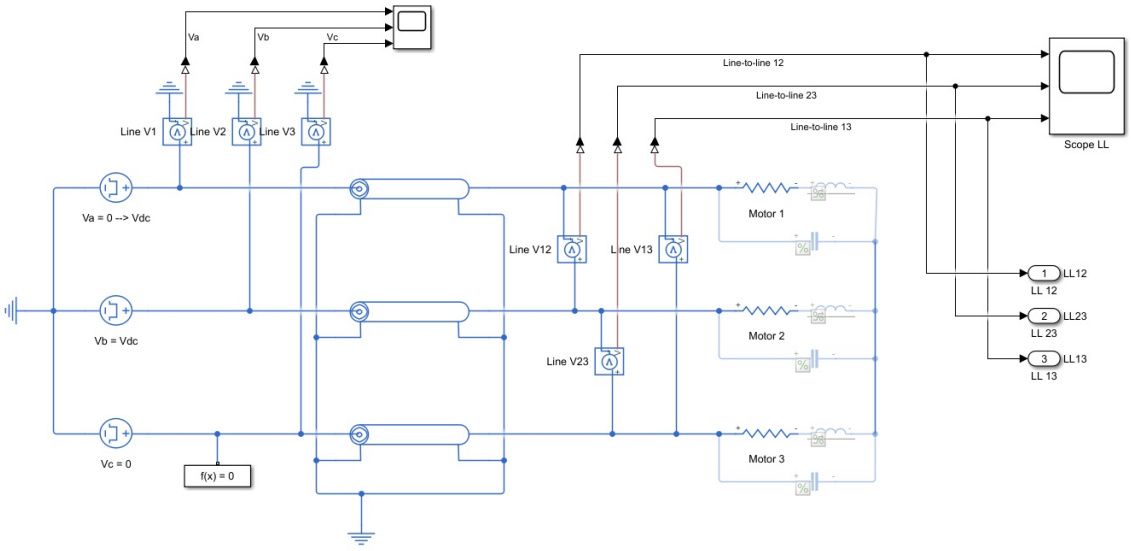

Figure 3.5: Simscape Simulink model of the 3-phase feeder cable and motor.

A short MATLAB script is used to define all parameters described in Table 3.1. Upon execution, the script saves all variables into a shared Workspace with Simulink, which in turn has all variables mapped to the appropriate components. Afterwards, it calls the execution of the Simulink file which runs the simulation, shows the resulting voltages on a scope and also saves them in the same Workspace. This will show the oscillating overvoltage produced in the motor terminal.

Furthermore, the MATLAB code runs a loop that progressively changes the input cable length l of the distributed transmission lines, while holding the rise time t_r constant. This process is repeated for several t_r to check the dependence of peak voltage values on the cable length and rise time. This will corroborate or disprove the literature results in Eq. 3.20, 3.22 and Figure 3.3.

3.3. Results

In the first instance, the 1-phase model shown in Figure 3.4 is run at a voltage step of $V_{dc} = 200$ V, with a cable length of 4 m and a rise time of 100 ns. Through simple calculation based on Table 3.1, the propagation time of the transmission line is found in Eq. 3.24:

$$t_p = \frac{l}{u} = l\sqrt{LC} = 89.44 \text{ ns} \tag{3.24}$$

Figure 3.6 illustrates the source and terminal voltages at both end of the line. This $t_p = 89.44$ ns can be seen as a delay between the source voltage step and the initial increase in terminal voltage

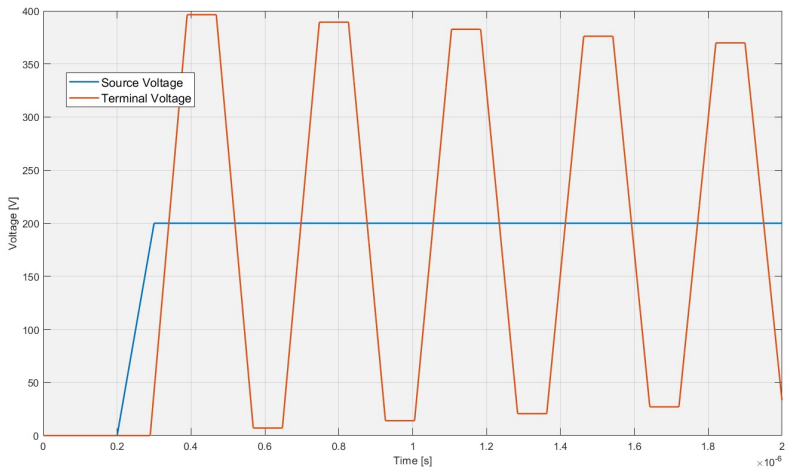

Figure 3.6: Source and terminal voltages measured using the 1-phase transmission line model in Figure 3.4.

First, the loop over the cable lengths is ran on both the 1-phase and the 3-phase transmission line models. The results are then compared to discard or confirm any possible differences between the two arrangements that could explain the discrepancy in literature. Figure 3.7 shows the peak terminal voltages measured for a range of cable lengths, using three different rise times of 75 ns, 100 ns and 150 ns on the 1-phase model. A regression is also run to more accurately examine the linear tendency of the peak voltage at lengths below the critical length. A similar process is done using the 3-phase model in Figure 3.8 for a 100 ns rise time.

Comparing both models, the 3-phase system presents a relevant amount of noise, likely caused by interactions between phases through the neutral point. However, the linear regression is and the critical length exceptionally similar to the previous case (at $t_r = 100$ ns) and the general behaviour is comparable. For these reasons, and for more simplicity, from now on only the 1-phase model is studied.

3.3.1. Critical Length and Cable Length Dependence

At this stage it can be noticed already that the regression equations do not resemble Eq. 3.20 nor Eq. 3.22. Instead, they show a bigger slope and a different *y-intercept*, reaching a minimum peak voltage at a finite length instead of a zero length claimed by literature. Moreover, the critical length can be found, according to von Jouanne [36, 37], following Eq. 3.21. As an example let us examine the $100ns$ case:

$$l_c = \frac{t_r}{3\sqrt{LC} =} = \frac{100 \times 10^{-9}}{3\sqrt{10^{-6} \times 500 \times 10^{-12}}} \text{ m} = 1.49 \text{ m} \tag{3.25}$$

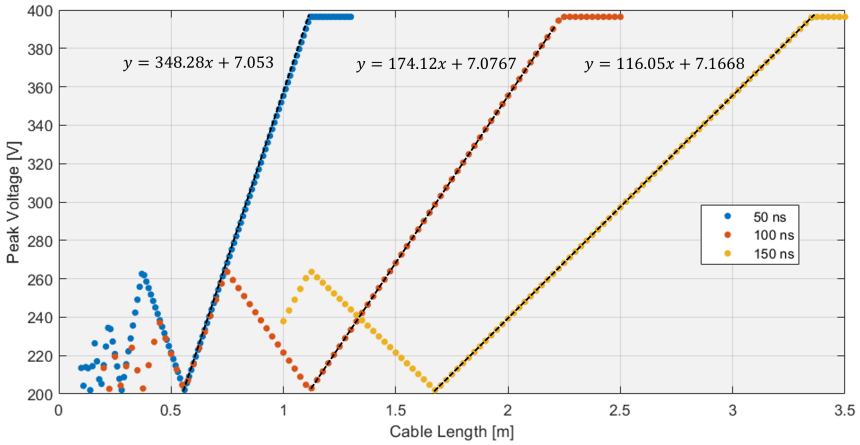

Figure 3.7: Peak voltage over different cable lengths using the 1-phase model, with various rise times. The equation of the linear region is shown.

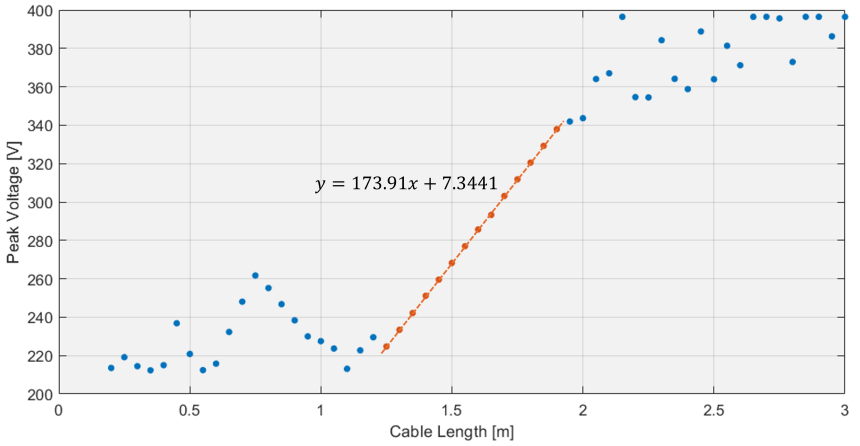

Figure 3.8: Peak voltage over different cable lengths using the 3-phase model, at a rise time of $100ns$. The equation of the linear region is shown.

This can be discarded by checking Figure 3.7, which shows the real value for critical length to be compliant with Eq. 3.23:

$$l_c = \frac{t_r}{2\sqrt{LC} =} = \frac{100 \times 10^{-9}}{2\sqrt{10^{-6} \times 500 \times 10^{-12}}} \text{ m} = 2.24 \text{ m} \tag{3.26}$$

This discrepancy is explained by the fact that during the first t_p the motor terminals have not yet received the voltage transient. By observing the Bewley diagram, the point drawn is that the reflections actually take $2t_p$ to make the round trip instead of $3t_p$, disproving Eq. 3.21.

Regarding cable lengths longer than l_c, Eqs. 3.20 and 3.22 hold true when describing the maximum voltage value, according to what has been studied in Section 3.1.1 through Transmission Line Theory. For shorter cables, nonetheless, both formulas fail to predict the points of minimum overvoltage, as well as the several smaller patters registered at smaller lengths.

In order to explain this discrepancy, a more in-depth analysis of the peak-voltage dependence on length is done. In particular, in Figure 3.9 it is noticed that the first minimum (closest to l_c) is found exactly at half the critical length. This point, hereby defined as optimal length l_{opt}, is found using:

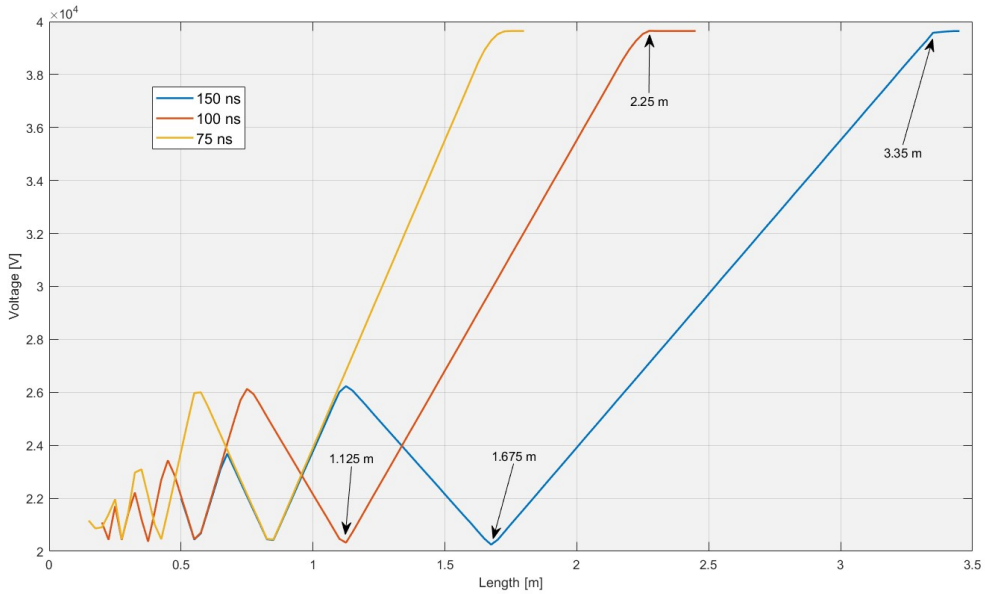

Figure 3.9: Value of critical lengths of the rise times under study.

$$l_{opt} = \frac{l_c}{2} = \frac{t_r}{4\sqrt{LC}} \tag{3.27}$$

To fully understand this situation, the 1-phase model is run with particular parameters ($t_r = 250$ ns and $l = 3$ m) to obtain a relatively small overvoltage. This is shown in Figure 3.10 where relevant timestamps are marked as *1, 2, 3* and *a, b, c*. Points *1*, *2*, and *3* are actually the same as the ones in the Bewley diagram in Figure 3.2. The timestamps in the graph are as follows:

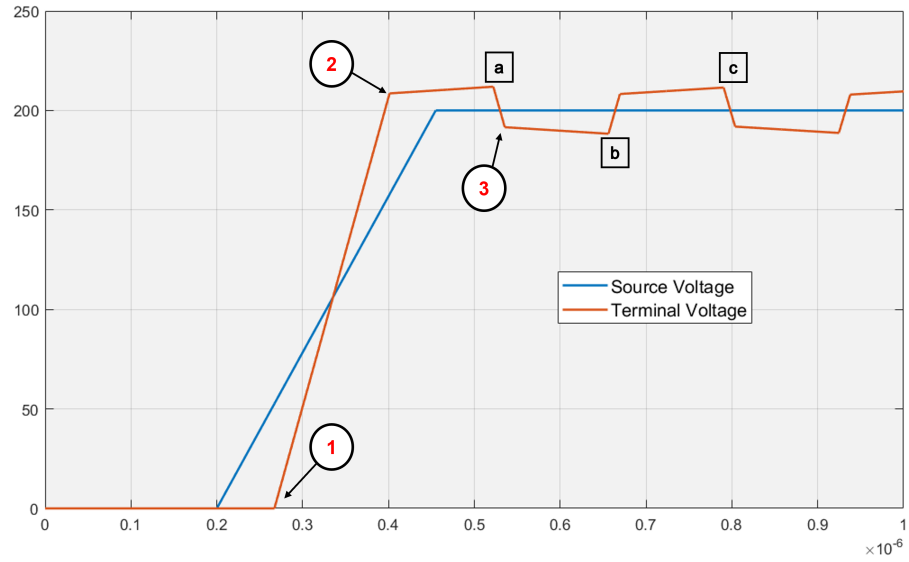

Figure 3.10: Source and terminal voltages measured using the 1-phase model at 250 ns and 3 m.

- ***1)*** The first t_p has passed and the source pulse V_{dc} reaches the terminal. Simultaneously, the first reflection V_1^- interferes with V_{dc}, raising the voltage.
- ***2)*** After $2t_p$ since point *1*, the first reflection V_1^- traveled to the inverter and back to the motor with an opposite sign as V_2^+. With such relatively long t_r, at this instant both V_1^- and V_2^+ are increasing and decreasing at similar rates, cancelling each other's growth. Note that a second terminal reflection occurs V_2^-.
  - ***a)*** At this point, a full t_r has passed since point *1*, meaning that V_1^- growth has stopped, hence V_2^+ dominates and the voltage decreases.
- ***3)*** After another $2t_p$ after point *2*, V_2^- makes another round trip inverting its sign to positive as V_3^+, completing a full cycle of the RWP.
  - ***b), c)*** Illustrate the repeating process that occurs in *a*.

Therefore, with relatively long rise times and short cable lengths, the reflections have time to travel back an forth, cancelling each other. In particular, if points *a)* and *3)* were to happen at the same time, the growth halt of a positive pulse is matched with the reach of the next positive pulse, while the same happens for negative pulses. Hence, the optimal length $l_{opt} = t_r/2u$ causes a constant state of destructive interference, effectively nullifying the RWP.

This analysis can also be applied to different rise times when the feeder cable length is fixed. Ultimately, the recommendation drawn from this chapter is to design a feeding system for the motor that complies with Eq. 3.27, effectively reducing the overvoltage from RWP to zero.

3.4. Alternative Mitigation Techniques

This section briefly introduces two more possibilities suggested in literature. Although these techniques fall outside the scope of this thesis, it is encouraged to explore the references and consider them in case of any design constraint that would impede the application of the optimal length previously mentioned.

3.4.1. Voltage Switching Polarity

Voltage Switching Polarity is studied by D'Amato et al. in their article on the *Impact of PWM Voltage Waveforms in High-Speed Drives* [6]. The main idea is to use unipolar switching as opposed to the more intuitive bipolar switching.

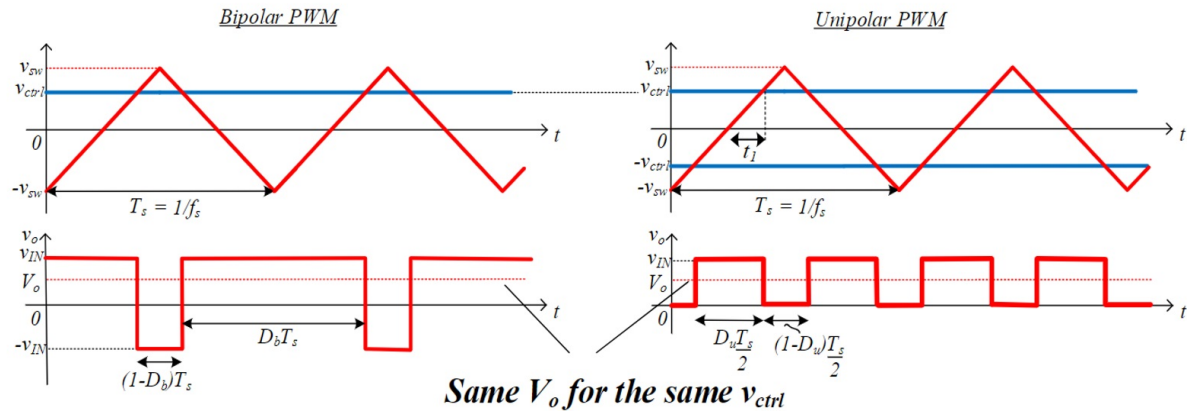

Figure 3.11: Basic explanation of the functioning of bipolar and unipolar pulse switching. Image taken from *Electronic Power Conversion* course ET4119 / SET3095, from TU Delft. [45]

Although this will in no way lessen the effects of RWP, unipolar switching generates pulses going from 0 to V_{dc}, thus having a voltage transient half as big as the one generated with bipolar switching (from $-Vdc$ to V_{dc} [46]. According to the study conducted by D'Amato, this choice significantly reduces the probability of PDs within the insulation, showing a higher voltage threshold. Figure 3.12 encapsulates the difference in lifetimes with these two techniques.

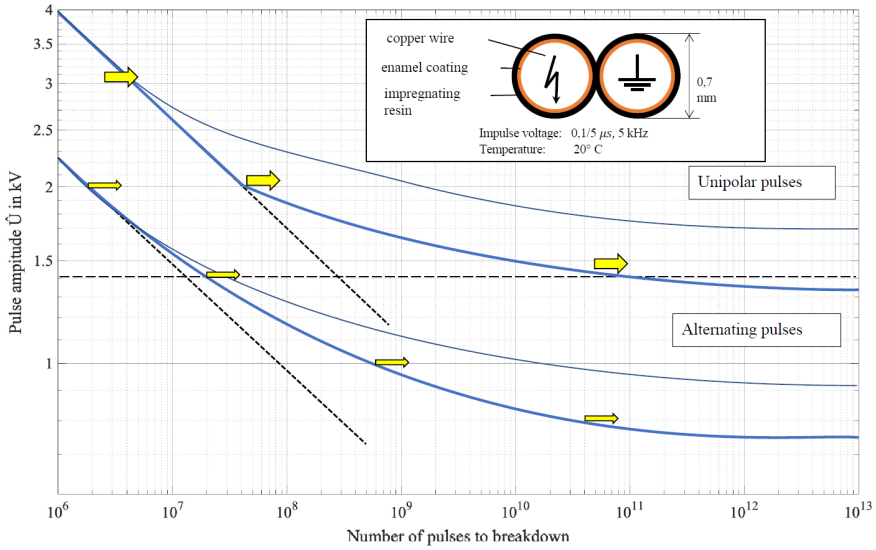

Figure 3.12: Study on the lifetime of insulation subjected to unipolar and bipolar switching.

On the contrary, it is relevant to consider their application in an AC machine. Bipolar switching is much simpler and robust to control a 3-phase motor drive. Unipolar switching produces positive (or negative) pulses and introduces the concern of a much more convoluted control [46]. The need for such complicated technique is not explored in this work, thus more investigation from the reader is encouraged to decide the viability of unipolar voltage switching.

3.4.2. RLC Filters

Besides the appropriate design of inverter rise times, Robert W. Maier and Mark-M Bakran propose the use of RLC filters to reduce the overvoltage caused by reflection in the feeder cable [41]. Two possible options are presented, an RLC du/dt filter at the inverter side, before the transmission line (see Figure 3.13a); and an RC filter at the terminal side, after the transmission line (Figure 3.13b). Their article also shows a comparison between their performance.

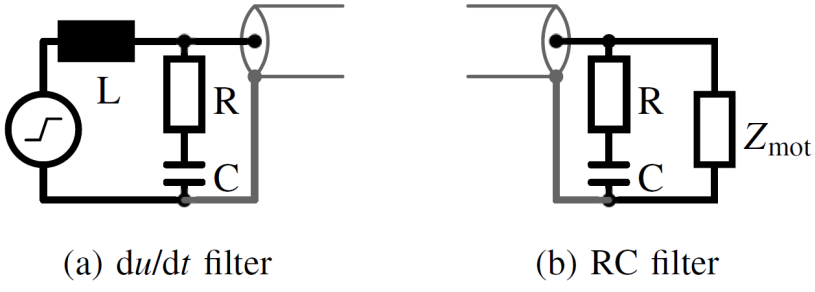

Figure 3.13: Two filter options for the transmission line, proposed by Robert W. Maier. [41]

All in all, the use of a filter in the application of aviation is, nonetheless, discouraged in this thesis. This is due to the extra weight that the filters will introduce to the system [42], which should instead be

minimized. Only if other mitigation techniques are not viable or fail to significantly reduce overvoltages, this option should be considered.

For the sake of completeness, however, a short paragraph is dedicated to the possible benefits of this method. The model displayed in Figure 3.4 is slightly modified to include the filters as (Figures B.1 & B.2) at the corresponding ends of the transmission line as shown in Figure 3.14. The RLC dv/dt filter is included at the inverter side, whereas the RC filter is at the motor terminal side.

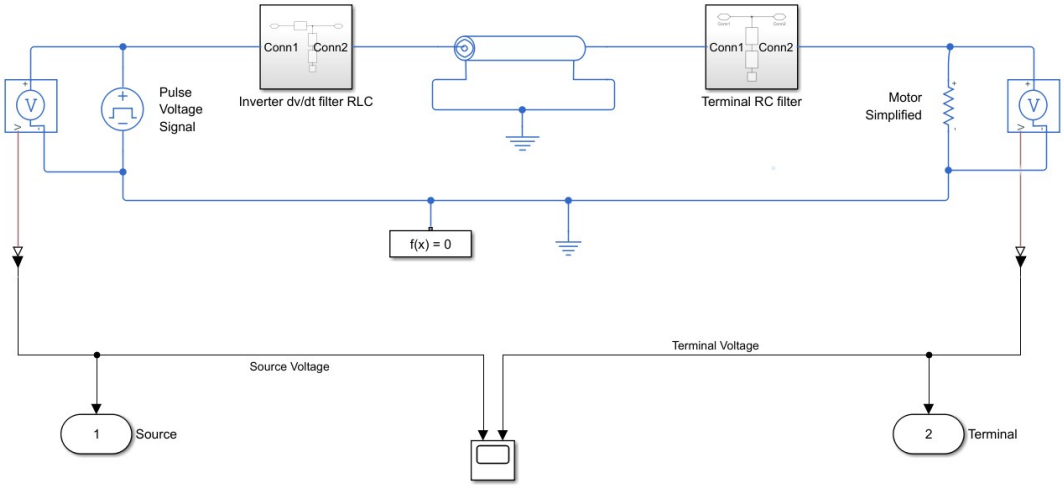

Figure 3.14: Transmission Line model with corresponding voltage filters.

Both filters are tested independently, and their outputs are shown in Figures 3.15 and 3.16. At this stage, the literature for the usage of voltage filters has not been reviewed in depth. Due to this, the parameters of the lumped elements of the filters are directly based on the filters proposed by Annette von Jouanne in [37], and listed in Table B.1. When compared to the original overvoltage result shown in Figure 3.6, the effect of the usage of these filters is negligible.

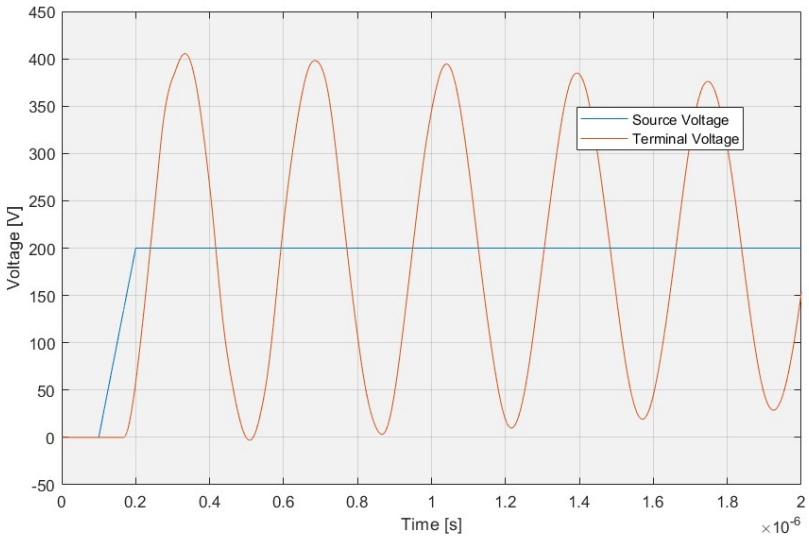

Figure 3.15: RWP voltage response when using only the RLC filter at the inverter side.

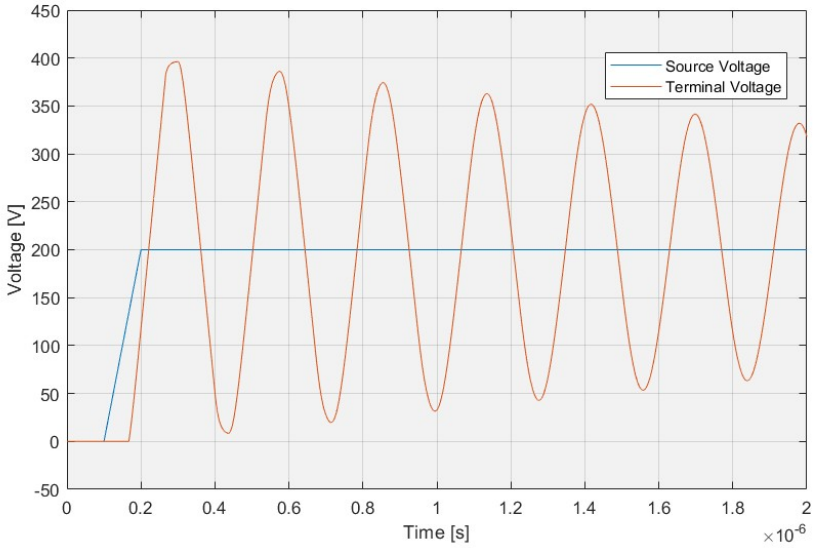

Figure 3.16: RWP voltage response when using only the RC filter at the terminal side.

It is relevant to note that von Jouanne reported much more optimistic results, likely due to a more proper filter design, well adjusted to the system characteristics. In order to realized similar results, the reader is encouraged to investigate more about voltage filter design.

3.5. Conclusion

A thorough literature review analyzed the theory presented by previous authors. First, the Transmission Line Theory was deeply studied in Subsection 3.1.1 in the context of this project. The basis of this theory was used to develop an appropriate model that could simulate the effects of the RWP, with the goal of achieving a basic understanding of the phenomenon and realizing a formula to mitigate its undesirable consequences.

During this literature review a critical discrepancy was found in the peak voltage resulting from the RWP (subsection 3.1.3). A necessary verification was carried out using Simulink to confirm or deny the validity of these formulas. To do that, a model was designed to exacerbate the effect, by adjusting its parameters to a hypothetical machine based on previous experiments and articles by authors such as [6, 10, 28, 40]. A series of rigorous simulations were done to expose the real response of the system given different rise times and cable lengths, yielding results that align with expectations from previous works like [6, 8, 32, 42].

A combination of these results and a deep understanding of the Transmission Line Theory analysis were used to develop a relationship between t_r and l. This relationship is backed up by simulation and aligns with the explanation given by D'Amato et al. [6]. It also disproves the formulas given [36, 37, 40, 41]. A careful investigation of the references of these papers revealed that their formulas were drawn from a common reference [36], which assumes a linear descent of the overvoltage value with rise time. This assumption has been, however, proved wrong.

4

Non-uniform Voltage Distribution

This chapter covers the overall behavior of the voltage waves inside the motor windings, and the modelling of the non-uniform voltage distribution that results. To do so, there is a short literature review in Section 4.1 that explores the theory behind the system and different modelling techniques to accurately represent it, as well as an experimental comparison of these techniques. Then, the methodology chosen for this thesis is portrayed and explained in Section 4.2, and the various results and casuistics found are presented in Section 4.3

4.1. Literature Review

Through a similar process of voltage wave propagation [47], many authors in the past have noticed another undesirable process occurs inside the stator. When applying a fast voltage transient dv/dt to the stator windings, by means of a reasonably fast PWM inverter system, the voltage is not equally distributed through the coil turns. Instead, the first couple of turns are subjected to a much bigger voltage drop, concentrating the voltage stress around that area of the slot [9, 48, 49, 50, 51, 52].

As opposed to the circuit simplicity of the RWP models studied in Chapter 3, the models that study the stator windings present many more variables and complications. The relative distance between each turn, and between them and the grounded stator, give rise to many parasitic effects such as capacitances and resistances [48]. Figure 4.1 shows the interactions that appear in such construction, including:

- Stray capacitive coupling to ground;
- Stray capacitive coupling between turns;
- Resistive interactions to ground;
- Resistive interaction between turns;
- Series resistance along the coil;
- Self and mutual inductances between turns.

Most authors, however, consider the turn and groundwall insulation to be ideal in these studies, thus ignoring the turn-to-ground resistance and turn-to-turn resistance [9, 53, 54]. In such a construction, the appropriate coil schematic is shown in Figure 4.2 with a simplified two turn design.

This setup if often applied to windings with a higher number of turns, making a complex network of RLC parameters (see Subsection 4.1.2). With such a model in mind, many authors noticed a decrease in the voltage uniformity along the turns as the rise time of the excitation voltage pulses decreases [49, 50, 51]. The higher frequency associated with these faster voltage transients dv/dt exacerbates the

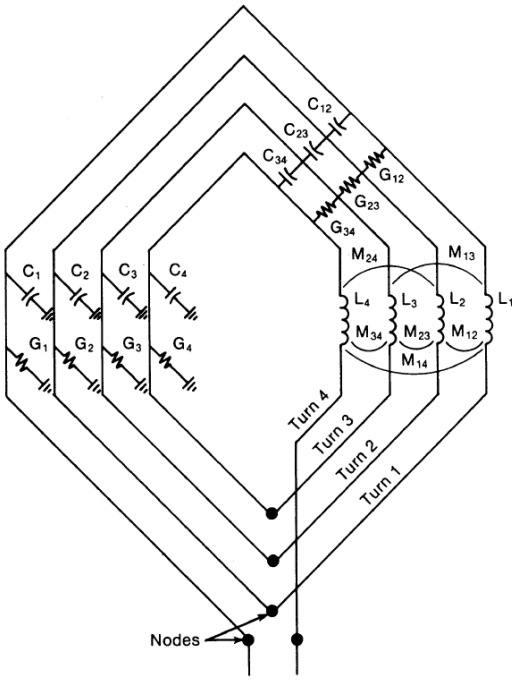

Figure 4.1: Coil schematic and circuit parameters from R.G. Rhudy et al. [48]

parasitic capacitances, and it is suggested that this capacitive coupling with ground C_g is responsible for the nonuniform voltage distribution [54], due to voltage leaks towards the core.

Some studies have focused on experimentation to clearly observe this phenomena [9], [48], [50], [51]. The experimental setups often consist of voltage measurements at different points along the coil, by connecting terminals in between the turns and measuring with respect to ground. Then the voltage drop in each turn is computed by appropriate subtractions, as registered in Figure 4.3 [50]. The results show a clear voltage spike in the first turn, followed by a maximum in the second turn, third turn, etc. with different magnitudes and a clear time separation, explained by the finite propagation speed of the spike through the heavily inductive and capacitive wire. The increased resistance at higher frequencies (due to skin effect, see Subsection 4.1.3) quickly dampens the oscillations until the voltage distribution evens out. Thus, the higher risk of PDs is at the first instants following the voltage transient.

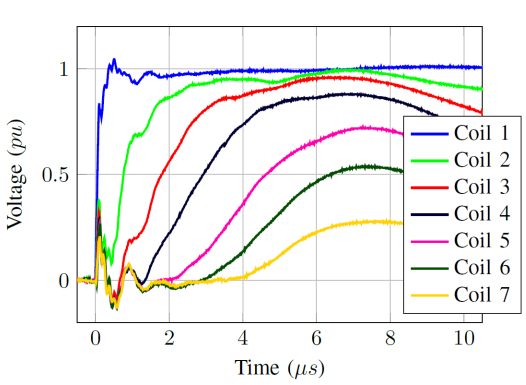

(a) Coil to ground voltage distribution.

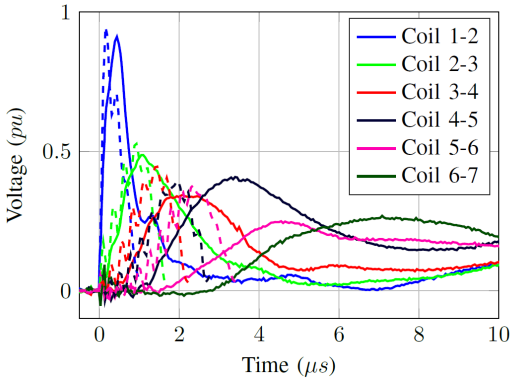

(b) Coil to coil voltage distribution.

Figure 4.3: Experimental voltage distribution from Krings et al. article [50]. The figure b) includes experimental data (solid line) and simulated data (dashed line) from their study.

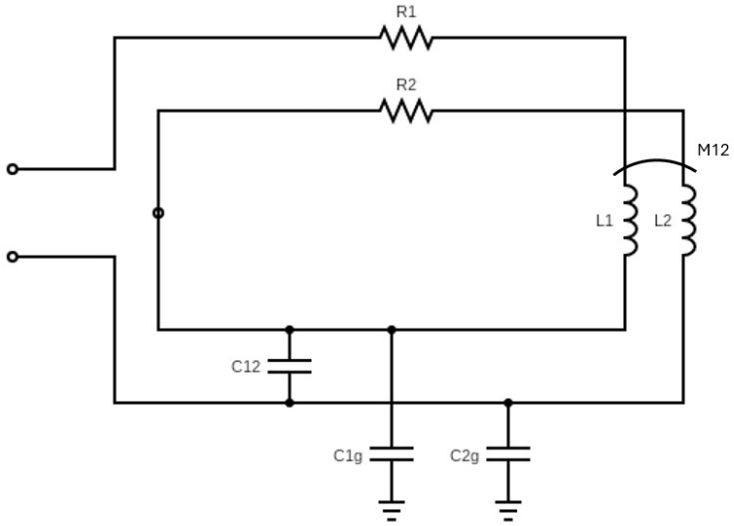

Figure 4.2: Simplified schematic of the equivalent circuit of a 2 turn coil.

There are many attempts in literature to replicate these results via simulation, with several different techniques and approaches. However, two main categories are recognized during the literature review:

- Multi-conductor Transmission Line Theory (MTL)
- Lumped/Distributed Parameter Equivalent Circuit

4.1.1. Multi-conductor Transmission Line Theory (MLT)

The multi-conductor transmission line theory is a generalization of the transmission line theory explored in Chapter 3. In this particular case the line consists of a bundle of separate conductors which represent each turn of the stator winding, divided in sections and appropriately connected at the ends.

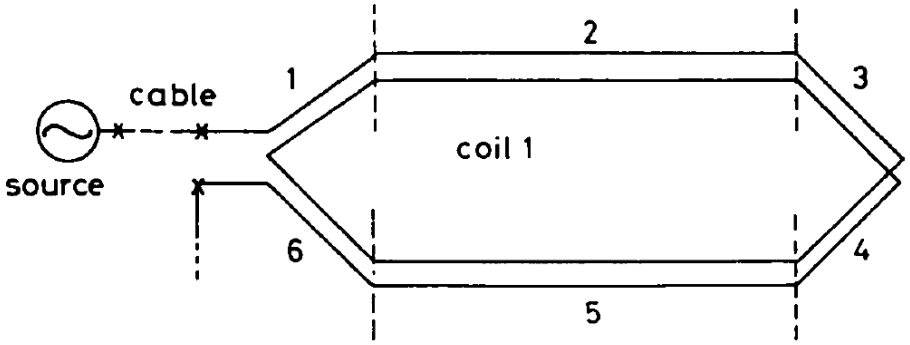

Figure 4.4: Representation of one coil with 2 turns, with 6 distinct sections.

In 1984, P.G. McLaren and H. Oraee [29] published a paper with a very clear explanation of this formalism. Considering the geometry and placement of a typical coil used in AC machines stators, seen in Figure 2.1a, two clear regions can be decided: the slot area and the overhang area. The wire presents different characteristics when wounded through each of these two regions, hence the separation showcased in Figure 4.4, divided by dotted lines. Areas 2 and 5 are inside the slot surrounded by the core; while 1, 3, 4 and 6 are in the overhang. This schematic can be unwrapped for a more comprehensive depiction of all the conductors present in this transmission line (two in Figure 4.5).

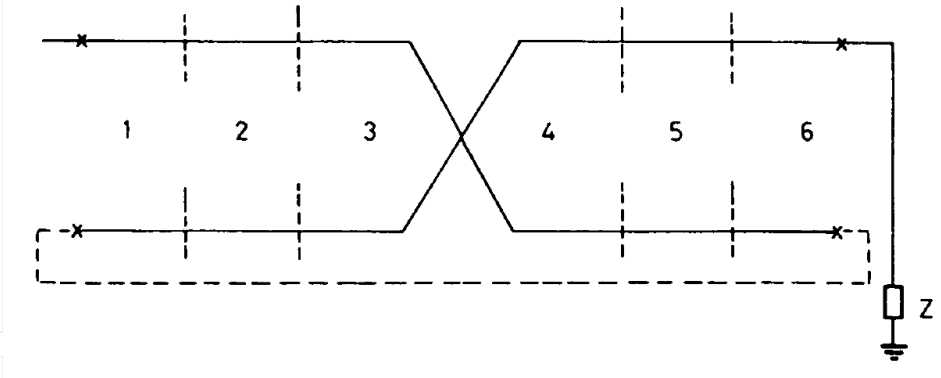

Figure 4.5: Schematic of the coil sections with an unwrapped coil.

As opposed to the single pair of equations used in Subsection 3.1.1, the presence of multiple sections within the problem means each one has their own voltage and current values, organized in column vectors. This implies the need for matrix calculus to solve a finite sized set of Telegrapher Equations [29, 47]. In the frequency domain, the Telegrapher Equations can be written as:

$$\frac{d}{dx}\overline{V} = -[Z]\overline{I} \tag{4.1}$$

$$\frac{d}{dx}\overline{I} = -[Y]\overline{V} \tag{4.2}$$

Where $\overline{V}$ and $\overline{I}$ are variable column vectors, $[Z]$ is the impedance matrix and $[Y]$ is the admittance matrix, both per-unit length. These are defined as [29]:

$$[Z] = [R] + j\omega[L] \tag{4.3}$$

$$[Y] = [G] + j\omega[C] \tag{4.4}$$

Where $[R]$ and $[G]$ are resistance and conductance matrices per-unit length. By cleverly differentiating these Telegrapher Equations, similarly to Eq. 3.5, they can be expressed as wave equations such as:

$$\frac{d^2}{dx^2}\overline{V} = [Z][Y]\overline{V} \tag{4.5}$$

$$\frac{d^2}{dx^2}\overline{I} = [Y][Z]\overline{V} \tag{4.6}$$

In order to solve these equations it is mandatory to either measure or simulate all the elements in the parameter matrices $[Z]$ and $[Y]$, including resistances, capacitances and inductances. Then the solutions can be found by defining the proper boundary conditions, such as equating the voltages at the section interfaces, and accounting for the input voltage pulse.

$$V_1(x = d) = V_2(x = 0) \tag{4.7}$$

$$V_1(x = 0) = V_{terminal} \tag{4.8}$$

It is relevant to notice that this system of differential equations is heavily coupled and the solution process is far from trivial. Several steps in between need to be taken, like adequate variable substitution to uncouple the system [29].

4.1.2. Equivalent Circuit

This approach is more popular in literature, and consists on designing an equivalent circuit that can accurately model the interactions taking place inside the stator wiring. This model can then be simulated through several dedicated softwares such as MATLAB Simulink, PLECS or LTSpice. Many different circuits have been proposed with different levels of complexity, but most have the characteristic of dividing the coil in sections, each one representing one full turn of the coil [9, 48, 53, 54]. The turns are usually defined as a single inductor L_i, often in series with a resistor R_i, which interact with each other through a mutual inductance M_{ij} and a mutual capacitance C_{ij}, where i and j represent each turn/conductor [9, 54]. Also, the turns are always capacitively connected to ground through a C_{ig}. Some models can be observed in Figures 4.6, 4.7.

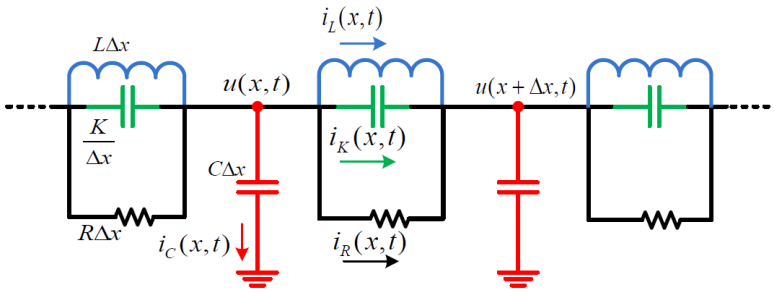

Figure 4.6: Simple coil model with RLC elements in parallel, and connections to ground. [53]

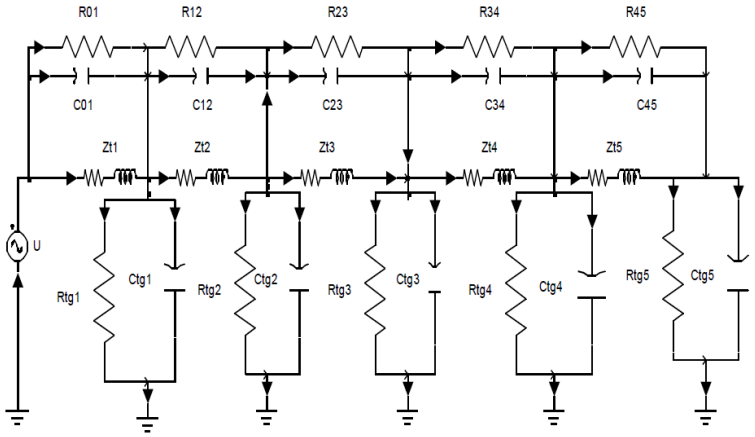

Figure 4.7: Coil model with a series-parallel disposition of series R-L with parallel C. This model also accounts for resistive losses of turn and groundwall insulators, in parallel to the capacitances associated. [9]

These models are simplified versions of the full picture, and offer practicality in exchange for accuracy. They account for just a first-neighbor interaction (closest conductor/turn to the one under observance) yet a more rigorous approach considers also the influence of all neighbors over every other [51, 54]. These other models include a mesh of connections between every single turn, which connect them through mutual inductances and capacitances regardless of their position within the slot. Some models may even divide each turn into smaller sections (similarly to the previous method) to account for any changes in the parameters, or to obtain finer results. The appropriate modelling of these circuits require the calculation of all the elements in the capacitance and inductance matrices, and the appropriate knowledge of the solving software to implement. Larger models with a high number of turns can become computationally expensive.

However, theory suggests a shielding effect between conductors due to their layout, which would significantly reduce the mutual capacitance between second and subsequent neighbors. This is later

confirmed in this thesis via simulation in COMSOL Multiphysics (see Subsection 4.2.3). Moreover, in addition to the reduced mutual impedance between far neighbors, the HF behavior of the circuit weakens the inductive influence in comparison to the strong capacitive and resistive reactions [54]. This might, to certain extent, mitigate the inaccuracies of the simplified models.

4.1.3. Parameter Calculation

Capacitance Matrix

Some studies proposed a straightforward calculation of capacitances by using a parallel-plate approximation, given the rectangular shape of conductors used in medium voltage, form-wound slots [9, 47]. These approximations often consider a shielding effect, making the capacitive coupling of 2nd or subsequent neighbors negligible. A comprehensive model is shown in Figure 4.8, where all the flat faces of the conductors have a capacitance with either ground or the closest neighboring conductor.

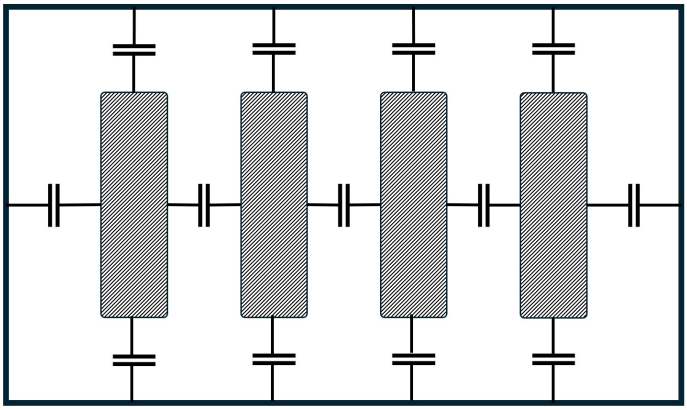

Figure 4.8: Capacitances acting within a 4 conductor rectangular slot, based on assumption made in [47].

In this scenario each one of the C values would have to be calculated by the parallel-plate capacitance formula:

$$C = \frac{\epsilon A}{d} \tag{4.9}$$

Where ϵ is the permittivity of the dielectric medium between the conductors, A is the area of the smaller surface in the coupling and d is the distance between the conductors. This assumptions are, however, very bold considering the small surface area of the wires in comparison with the distance between them [11]. This formulation also fails to accurately consider the space around the corners of a rectangular wire, therefore incorrectly calculating the ground capacitances in such area of the slot.

Instead, the values of capacitance needed for the implementation of the models are often obtained computationally through FEM softwares, and then stored in matrix form: the capacitance matrix. In a system with many separate conductors, every single one of them interacts capacitively with all the others, as well as with the ground [55]. The capacitance matrix relates the voltage of said conductors with the electric charge that their produce at their surface [56, 57], following Eq.4.10.

$$Q_i = C_{i0}V_i + \sum_{j \neq i}^{n} C_{ij}(V_i - V_j) \tag{4.10}$$

Considering the voltage V_i is essentially the voltage difference between the conductor and infinity, where the voltage is 0, C_{i0} is defined as the partial capacitance between conductor i and the ground

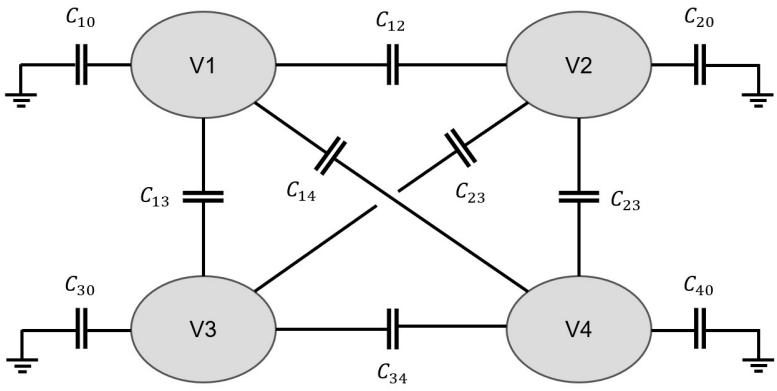

Figure 4.9: Schematic of 4 isolated conductors and the capacitances between them.

[51], whereas C_{ij} are the capacitances between conductors i and j. In a system with only 4 conductors, as illustrated in Figure 4.9, the equation to calculate the charge of the first conductor would be expressed as follows [56]:

$$Q_1 = C_{10}V_1 + C_{12}(V_1 - V_2) + C_{13}(V_1 - V_3) + C_{14}(V_1 - V_4) \tag{4.11}$$

Which can be rearranged in terms of the four voltages V_1, V_2, V_3, V_4, thus obtaining the following expression:

$$Q_1 = (C_{10} + C_{12} + C_{13} + C_{14})V_1 - C_{12}V_2 - C_{13}V_3 - C_{14}V_4 \tag{4.12}$$

From which the first row of the capacitance matrix, which defines the surface charge of conductor 1, is extracted. Following a similar approach for other rows, the Maxwell capacitance matrix is constructed as:

$$\overline{Q} = \begin{bmatrix} C_{10} + C_{12} + C_{13} + C_{14} & -C_{12} & -C_{13} & -C_{14} \\ -C_{21} & C_{21} + C_{20} + C_{23} + C_{24} & -C_{23} & -C_{24} \\ -C_{31} & -C_{32} & C_{31} + C_{32} + C_{30} + C_{34} & -C_{34} \\ -C_{41} & -C_{42} & -C_{43} & C_{41} + C_{42} + C_{43} + C_{40} \end{bmatrix} \overline{V} \tag{4.13}$$

Where each element outside of the diagonal represents the capacitance between conductors i and j, while the diagonal elements represent the self-capacitance under the influence of all other conductors. In order to obtain these values through finite element analysis (FEM), the Maxwell capacitance matrix is often rewritten through this formalism [10], where the first row is written for clarity as:

$$Q_1 = \lambda_{11}V_1 + \lambda_{12}V_2 + \lambda_{13}V_3 + \lambda_{14}V_4 \tag{4.14}$$

By comparing to Eq. 4.12, the method for extracting the capacitance becomes obvious. To obtain the mutual capacitances C_{ij}, one conductor must be excited at a non-zero voltage $V_i = 1V$, while all others must remain at zero $V_j = 0$ [10, 47]. Then by checking the surface charge of conductor j, created by the proximity to conductor i, their mutual capacitance is found. In this scenario, Eq. 4.14 becomes:

$$Q_j = \lambda_{ij} \times 1V + \sum_{k \neq i} \lambda_{kj} \times 0 = \lambda_{ij} = -C_{ij} \tag{4.15}$$

On the other hand, since the self-capacitance λ_{ii} is the addition of the ground capacitance plus the mutuals, it can be found by exciting every single conductor at $1\ \mathrm{V}$, while keeping the core grounded. Then the surface charge in a certain conductor i becomes [58]:

$$Q_i = \lambda_{ii} + \sum_{j \neq i} \lambda_{ij} = (C_{i0} + \sum_{j \neq i} C_{ij}) - \sum_{j \neq i} C_{ij} = C_{i0} \tag{4.16}$$

This can be easily achieved through simulation using the Electrostatics (*es*) module in COMSOL Multiphysics, where the electric potential can be independently defined for each element. Alternatively, another method can be used by computing the electrostatic energy stored in the system using a similar electric configuration [47, 59]:

$$W_j = \frac{1}{2} \sum_{i \neq j} C_{ij} V_j^2 \tag{4.17}$$

Before carrying out all these calculations, some details need to be accounted for depending on the model proposed. For instance, in complicated models where the coil is divided in sections (such as McLaren's version of MTL [29]), the overhang area is assumed to have no capacitance to ground [10].

Inductance Matrix

Similarly to the capacitances, the inductances can also be stored in matrix form of similar shape. Using COMSOL Multiphysics, several coils can be defined using the magnetic fields *mf* module. With it an independent current can be forced through each one, generating a magnetic field that interacts with the rest. The total inductance of a coil is defined as:

$$L_i = L_{ii} + \sum_{j \neq i} M_{ij} \tag{4.18}$$

Following a similar process as before, the self-inductance L_{ii} can be found by forcing a current of $1\ \mathrm{A}$ through one coil, while keeping the rest at zero. Correspondingly, to calculate the mutual inductance M_{ij} between i and j it is necessary to flow $1A$ through conductor j, while keeping the rest a zero, including i. COMSOL Multiphysics includes a function in the post-processing phase of magnetic field *mf* that can calculate these inductances by selecting conductor i.

However, the models required to calculate these parameters can prove to be quite complex and computationally heavy, possibly raising convergence error in the software. Another method proposed by many authors skips this step and claims that the whole calculation can be done with the computation of the capacitance matrix alone [47, 60, 61]. Considering the propagation speed through the wire, defined as:

$$u = \frac{1}{\sqrt{\mu \epsilon}} = \frac{1}{\sqrt{LC}} \tag{4.19}$$

The inductance and capacitance matrices are related through:

$$[L] \times [C] = \epsilon\ \mu\ [I] \tag{4.20}$$

Where $[I]$ is the identity matrix. The permeability of dielectric used in insulation are typically the same as free space, μ_0. Due to this, and since the inductance depends on the permeability of the surrounding medium [47], it is possible to calculate the matrix $[L]$ by computing the capacitance matrix in free space as a middle step, substituting the insulation with air. In this situation, the inductance matrix is:

$$[L] \times [C_0] = \epsilon_0 \mu_0 [I] \tag{4.21}$$

This method significantly reduced the computation time necessary to obtain all parameters of the system. However, it propagates any errors introduced by assumptions or approximations taken when calculating the capacitance matrix. Morever, considering the propagation speed is not constant over the course of the coil, the validity of this formula is not fully understood in this thesis, and more investigation is encouraged. In this work, the inductances will be manually calculated through FEM in COMSOL, assuming the inconveniences that it raises.

Resistance: Skin Effect and Proximity Effect

Beyond the simplicity of DC resistance, conductors in high-frequency tend to behave differently. It has been widely observed that current tends to flow closer to the surface of the conductor as frequency increases, giving rise to what is known as 'skin effect' [9, 62, 63]. This phenomena generates a smaller area for current to flow, resulting in a higher overall resistance as understood from its usual definition of in terms of the material resistivity (Eq. 4.22).

$$R = \rho \frac{l}{A} \tag{4.22}$$

Where ρ $[\Omega \mathrm{m}]$ is the material electric resistivity, l $[\mathrm{m}^2]$ is the length of the wire and $A[m^2]$ is the area of the cross section through which the current flows. The skin effect arises because of the magnetic flux produced by the AC current flowing through a conductor, which in turn generates eddy currents I_w inside of itself. This eddy currents follow the same direction as the AC current close to the surface, but opposite closer to the center [62], adding and subtracting accordingly as shown in Figure 4.10.

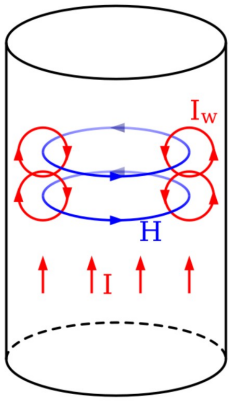

Figure 4.10: Schematic of the eddy currents I_w produce in a wire by the magnetic field H.

As a first approximation it can be assumed that the current flows in a cylindrical shell around the edge of the wire [63], thus the resistance would be:

$$R_{AC} = \frac{\rho l}{\pi r^2 - \pi (r - \delta)^2} \tag{4.23}$$

Where δ is the 'skin depth'. This parameter is defined as the depth at which the current density of the conductor has attenuated below $1/e$, or approximately 0.37 [64, 65]. The current density of the wire typically falls exponentially when approaching the center, following Eq. 4.24.

$$J_z = J_0 \, e^{-z/\delta} \tag{4.24}$$

Where z is the distance from the edge of the conductor, and the skin depth δ is:

$$\delta = \sqrt{\frac{2\rho}{\omega\mu_0\mu_r}} \tag{4.25}$$

Where μ_r is the relative permeability of the material (1 for copper [62]). This description is valid for infinitely wide flat conductors, and lack accuracy for widths similar (or smaller) than the skin depth, as well as for sufficiently small round conductors. Moreover, the time varying magnetic field induced not only affects the same wire, but also all other wires in close proximity to it. This is known as the 'proximity' effect' [66].

Given two parallel wires that carry current in the same direction, the magnetic field induced by the AC current creates eddy currents in each other, pushing the current density to those parts of the conductor that are the farthest apart [62]. This effect superposes with the skin effect, resulting in non-uniform current distributions around the wire cross sections, as can be seen in Figure 4.11.

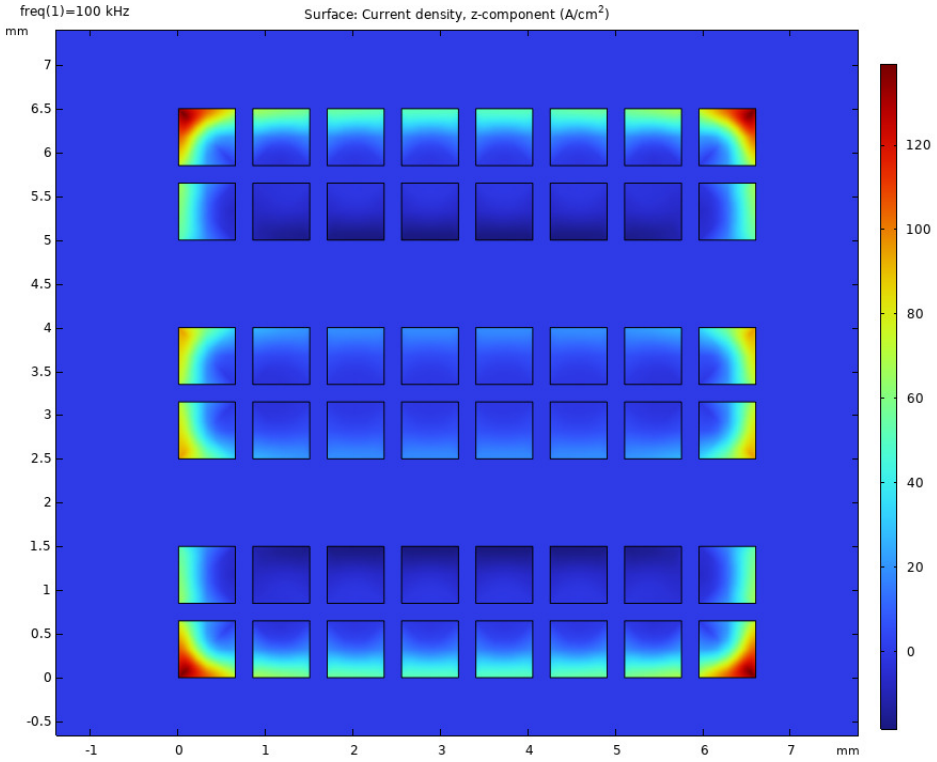

Figure 4.11: Visualization of current density through 3 conductors at a close distance of 1 mm, with an AC current at 100 kHz. The superposition of the skin & proximity effects can be appreciated. Simulated through COMSOL.

Due to the complexity of this problem, the dependence on the conductor geometry and placement within the slots, the analytical calculation of the resistance becomes non-viable. Instead, the computation can be done through simulation in COMSOL Multiphysics, where the same current is forced through all the conductors at the corresponding frequency. This software can accordingly calculate the current density around the cross section in a 2-D simulation.

It can be noted that the three conductors in Figure 4.11 are not solid. That is because in order to minimize the resistance introduced by the skin effect, often the conductors are separated in smaller insulated strands, or 'stranded' [11]. This is cleverly done to reduce the inside cross section through which the current density cannot flow, and is specially relevant in medium to high voltage machines.

4.1.4. Method Comparison

Under a rigorous study, it is clear that both methods (MLT and Equivalent Circuit) require essentially the same input parameters to compute results: resistance/conductance in each section, and the corresponding inductance and capacitance matrices. Therefore the parameters calculation does not play a role in the method decision.

It has also been shown experimentally in a comparative analysis by B. Oyegoke [63] that both methods discussed offer fairly similar capabilities and results, making them both perfectly suitable for this thesis once proper modelling is accomplished. For these reasons, the choice of methodology comes down to preference and/or practicality.

Whereas the MLT method offers an very clear and concise mathematical expression, as well as a very fast computing time, the complexity of solving so many coupled second order differential equations makes this problem non-trivial. On the other hand, albeit computationally expensive under certain rigor, the design of an accurate Equivalent Circuit is more practical due to the availability of softwares that can solve these problem, such as Simulink, PLECS or LTSpice. For these reason an Equivalent Circuit in Simulink is chosen in this thesis over the MLT matrix calculations.

4.2. Methodology

The main goal of this chapter is to accurately replicate the results observed in literature [10, 48, 54] regarding the uneven voltage distribution along the turns in the stator windings. This will be done computationally via simulation in MATLAB Simulink, as well as experimentally in order to verify the model by comparing results. Considering the previous discussion, the chosen method for the simulated study is an equivalent circuit model that will be based in the experimental setup.

4.2.1. Experimental Setup

Despite the fact that the object of this thesis is a medium-high voltage machine, the voltage distribution can be studied in a smaller machine using the resources available in the faculty. TU Delft provided a small laminated stator core with 12 salient poles around the inside perimeter, creating 12 slot-like regions between them. The dimensions of the core can be seen in Table 4.1.

Outside Diameter	D_{out}	138 mm
Inside Diameter	D_{in}	123 mm
Perpendicular Depth	d	49 mm
Pole Height	H	20 mm
Pole Width	W	10.5 mm

Table 4.1: Dimensions of the stator core use in experiments.

Several different wires are also provided, such as a section of flat copper wire suitable for form-wound coils. However, the reduced size of the motor makes very narrow slots, and given the lack of proper equipment the wires must be winded by hand, which has proven to be extremely difficult. As a result, a very irregular and lackluster coil caused the discard of this wire. Instead, the RS-PRO 357-744 wire is used [67]. This circular copper wire with enamel insulation has a diameter of 0.5 mm, making it outstandingly ductile and easy to wind around the poles. Nonetheless, its enamel coating is extremely fragile and prone to scratches that could compromise the connection reliability. In addition, the diameter of the cable is too small to accurately represent the interactions of a form-wound coil. To solve these issues, some assumptions need to be taken for an alternative approach.

It is hypothesised that the parasitic capacitance to ground may be mainly responsible for the non-uniform voltage distribution across the turns, since in high-frequency operation a relevant part of the input voltage might be leaking to ground through them. The test setup is designed with this idea in mind, where the conductors must be close to the core to replicate the non-uniformity. In order to imitate a simple 3 turn form-wound coil, such thin cable is winded many times into a 'mini-coil' around a pole, where each one represents a turn of the form-wound stator concept. This is done assuming that the voltage drop through a single turn of the thin wire is negligible. To maximize the coherence, a mini-coil is formed with 20 turns of the thin wire, one on top of the other in a line, keeping all of them at the same distance to the core. Due to lack of space in the slot, these 3 mini-coils are winded around 3 different poles, assuming the mutual capacitance between them to be small compared to the series capacitance of each one of them. In order to protect the insulation from scratches with the steel core, some adhesive tape is used. In addition, the laminated core is wrapped in electric tape to more easily connect it to ground during the experiment. The whole construction is shown in Figure 4.12. The mini-coils, henceforth known as just coils, are numbered as 1, 2 and 3.

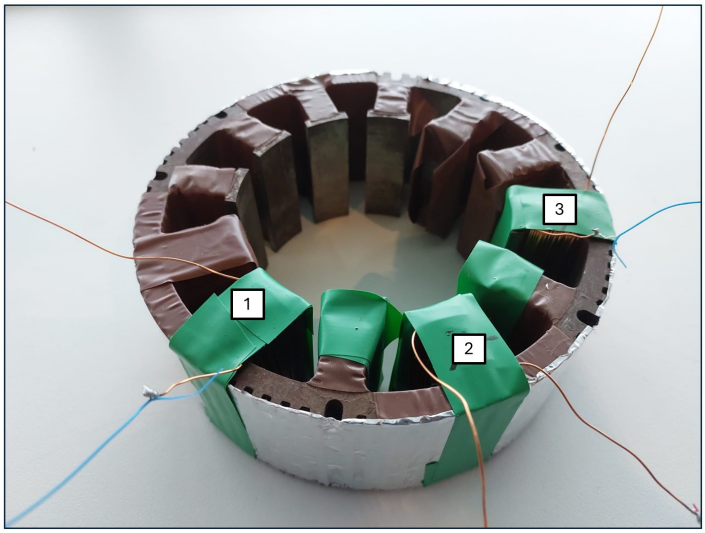

Figure 4.12: Picture of the stator core used in the experiment, with the corresponding 3 coils winded.

Coils 1, 2 and 3 are connected in series to one another creating the whole wiring. The beginning of coil 1 and the end of coil 3 are connected to a power source that supplies a square pulse voltage waveform with a rise time of 25 ns, while the sections of the cable in between each coil is converted into a terminal where probes can be connected (points 1 and 2). The core and the end of the wiring are both grounded, and probes are distributed like follows:

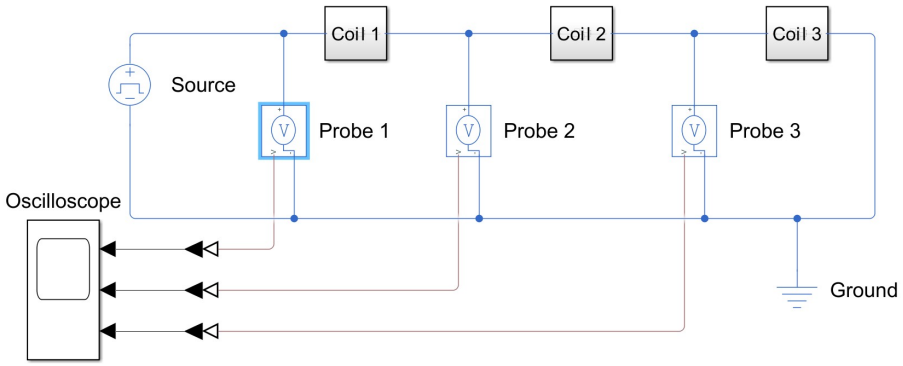

Figure 4.13: Schematic of the experimental setup and corresponding connections.

- Probe 1: connected to both ends of the wiring, in order to measure the terminal voltage.
- Probe 2: connected to terminal 1 (between coils 1 and 2), and to ground.
- Probe 3: connected to terminal 2 (between coils 2 and 3), and to ground.

The probes take the measurements to an oscilloscope, from which data can be extracted for post-processing. The whole experimental setup is shown in Figure 4.13.

4.2.2. Simulation Setup

The model build in MATLAB Simulink offers a pretty simplistic representation of the experimental setup, based on the most common RLC equivalent circuit of an inductor [68], with resistance, inductance and a series capacitance (see Figure 4.14). It also includes the corresponding capacitive interactions to the grounded core at both ends of the circuit, similar to a PI-section line. This is hereby defined as coil model.

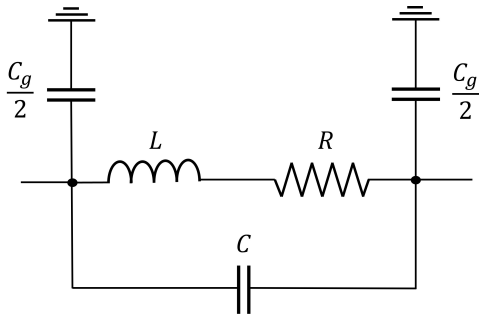

Figure 4.14: Simple schematic of an inductor/coil model with capacitance to ground.

Three of these elements are connected in series to one another, while also interacting via mutual inductance. Both ends of the circuit are connected to ground and to a pulse voltage source block respectively, where the latter emits a single square pulse, with a voltage transient dv/dt of $10\ \mathrm{V}$ and a rise time of $25\ \mathrm{ns}$, similar to that one sent by the real source in the experimental setup. The voltage is then measured using sensors and sent to a scope for visualization. The full setup is shown in Figure 4.15, and is hereby defined as circuit model.

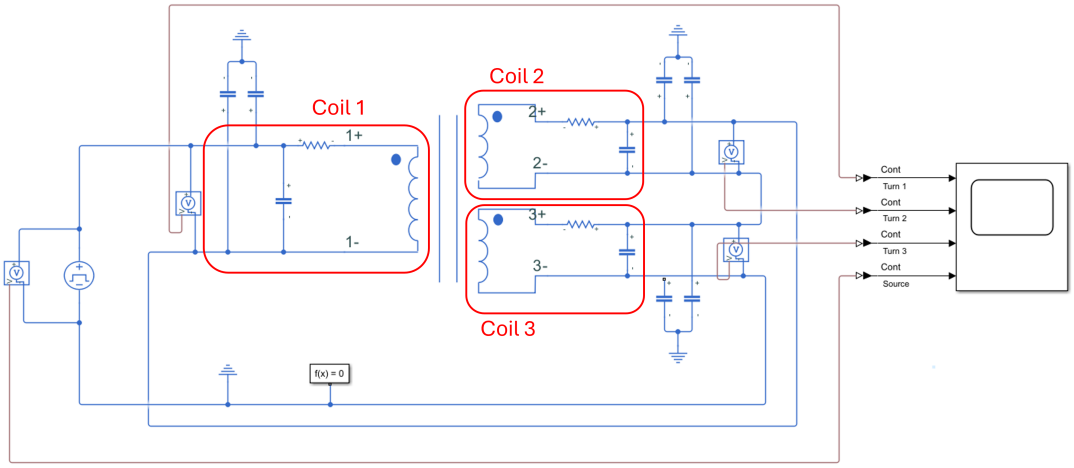

Figure 4.15: Full Simulink model of the three coils wounded in the stator poles.

It is worth noting that all element used in this model use lumped parameters as opposed to distributed. This choice, although sub-optimal for accuracy, has been taken due to the computation expense of distributed parameters in this software in order to avoid any divergence complications. As mentioned in Subsection 4.1.2, the passive elements in the circuit needs their appropriate values, which cannot be calculated analytically. Instead, they depend on the materials and geometry of the system. The corresponding values R, L, and C can, once again, be obtained both via simulation and through real-life measurements. Both methods were used in this thesis to account for their advantages and disadvantages.

4.2.3. Parameter Determination through Simulation: COMSOL Multiphysics

The RLC parameters of the wire are mostly dependent on the materials of the conductor, insulation and stator core, as well as on their geometry and placement. COMSOL Multiphysics has the capability to accurately replicate them through 2D and/or 3D renders, its built-in material properties and its physics simulations solvers for electrostatics and electromagnetism. While it offers the advantage of practicality and versatility and expandability, it can be difficult to properly replicate the real case, considering the irregularities born during the hand-made setup.

Three separate models are drawn to calculate separately the inductance matrix $[L]$ of the three coils, the capacitance matrix $[C]$ and the series resistance R of each coil.

Capacitance Computation

Before the first set of capacitances is calculated, a quick comparison is run between the parallel-plate analytic approximation and the FEM simulation. Using a convenient rectangular slot with 6 rectangular conductor placed inside, both methods (discussed in Subsection 4.1.3), are used as shown in Appendix A as well as the results from approximation (Matrix A.1) and FEM simulation (Matrix A.2). While the shielding assumption is fairly precise, and the parallel-plate formalism generally works for close, flat surfaces, it does not provide the desired accuracy for the areas around curved conductors or corners, necessary for the computation of ground capacitance. Hence all efforts are dedicated to COMSOL simulation.

Due to the separation between the wired poles no capacitive interaction is considered between the coils. Therefore, the simulation only represents a single pole wired with its respective coil. A 2-D model is adequate to compute values of capacitance per-unit length (see Figure 4.16), considering the stator and cable dimensions displayed in Table 4.1. The distance between two consecutive turns is estimated to be around half the diameter of the cable, thus $0.25\ \mathrm{mm}$ considering the enamel thickness, while the distance to the core is measured at around $0.55\ \mathrm{mm}$.

To calculate the capacitance to ground, the process previously explained is put into practice, where the capacitance between two elements is the relationship between their voltage and the surface charge created. In this case, the whole coil is considered a single conductor and fixed at $1\ \mathrm{V}$, while the stator core is grounded. By virtue of Eq. 4.10, the capacitance per-unit length is found by computing the surface charge of the stator core.

Conversely, whereas this operation is also valid for the series capacitance, the sheer amount of conductors in this case would imply repeating this process $n \times n$ times, making it unpractical. Instead, the electrostatic energy stored in the system is a much faster solution. Since the capacitance under study concerns the full coil, it is possible to apply a voltage to it as a whole by distributing the potential in each conductor according to their corresponding turn, like so:

$$V_i = i\ \frac{V_{total}}{n} \tag{4.26}$$

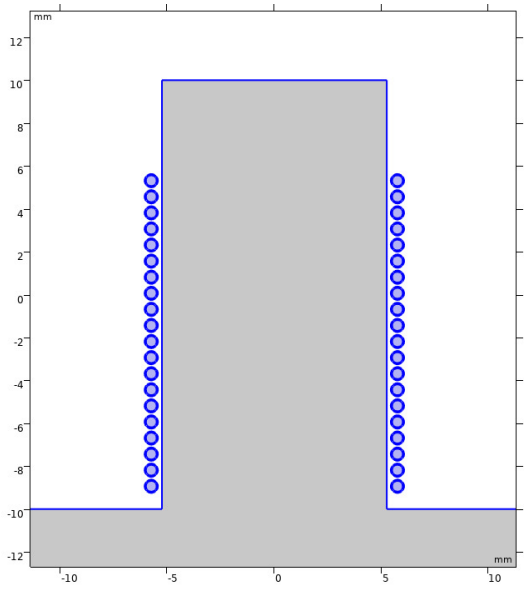

Figure 4.16: COMSOL 2-D model representing the cross section of a single pole of the stator, surrounded by the 20 turns that compose the coil.

Through COMSOL the electrostatic energy stored in the system W can be computed, and following Eq. 4.17 the total capacitance can be found. However, this value contains all the capacitive interactions in the system, including the ground. It is also necessary to separate series and ground capacitances in compliance with the inductor model in Figure 4.14. To do so, the condition of grounded stator has to be disabled. In this situation the solver can interpret the core to simply be part of the surrounding medium.

Inductance Computation

The theory behind the inductance calculation is trivial. The spatial distribution of the coils requires the consideration of all self and mutual inductances, coupling all three. A current of $1\ \mathrm{A}$ is forced through the first coil, while the rest have no current flow. In this situation, the magnetic flux felt by all conductors is solely produced by the first, thus allowing the measurement of self-inductance of the first coil and the mutual inductance with the other two. This process is repeated for each case using a Stationary Coil Geometry Analysis.

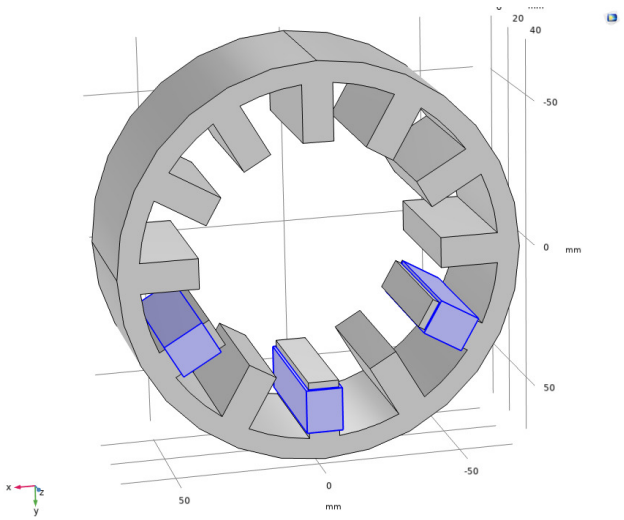

Figure 4.17: COMSOL 3-D model of the stator with homogenized multi-turn coils.

Although conceptually easy this is done via 3-D simulation, which is very computationally expensive and may arise convergence errors. To simplify the model, and since the magnetic flux is generated by the whole coils, they are modelled as a single block around the pole by using the 'Homogenized multi-turn' option with 20 turns. Moreover, since the permeability of the steel core is much higher than that of air, the space between the cable and the core is ignored in order to prevent improper mesh elements within it.

Resistance Computation

As previously mentioned, the geometry and distribution of the coil and the stator is too complex for analytical calculation of the skin and proximity effects. Instead, the per-unit length resistance can be calculated in COMSOL with a Frequency Domain Study, using the Magnetic Field (mf) module. All conductors are given a current of $1\ \mathrm{A}$ in the same direction, which should generate enough magnetic flux at high frequencies to generate these phenomena. Then, the simulation is run and the results are post-processed using the built-in function for 'Coil resistance (AC)', which in a 2-D model returns the resistance per meter of a particular conductor. The summation of all the resistances of each turn, times the length of each one results in the total resistance of the coil at a certain frequency.

$$R = W\ d\ \sum_{i}^{20} R_i^{pu} \tag{4.27}$$

4.2.4. Parameter Determination through Measurement

Firstly, the ground capacitance can be easily obtained by short-circuiting the wiring to dissipate any charge imbalance, and then connecting a capacitance meter to the wire and to the core. This will return the total ground capacitance of the full wiring, including the 3 coils. To approximate each coil's ground capacitance, it can simply be divided by 3 assuming all coils have an almost identical geometry.

On the contrary, the measurement of all other parameters cannot be done directly given the complexity of the system inside the stator. Instead, only the impedance and the phase angle of the full coil can be acquired using an Impedance Analyzer in the laboratory. Then, adjusting the inductor model explained in Figure 4.14 the coil impedance can be calculated by equating the equations to the results. The total impedance of the inductor is as follows:

$$Z = \left((R + j\omega L)^{-1} + j\omega C \right)^{-1} \tag{4.28}$$

Through some calculus the impedance can be expressed as a standard Cartesian complex number:

$$Z = \frac{R}{(1-\omega^2 LC)^2 + (\omega CR)} + j\frac{\omega L(1-\omega^2 LC) - \omega CR^2}{(1-\omega^2 LC)^2 + (\omega CR)} \tag{4.29}$$

Using the impedance analyzer, the frequency response of each coil is acquired, returning a wide spectrum of impedance and phase angle in terms of frequency. This is observed in a logarithmic scale in Figure 4.19 in order to localize the first peak, corresponding to the first resonance frequency of the coil. However, these spectrums are too wide and the high frequency values are too far scattered. Therefore a finer measurement is done in a smaller range close to the previously found resonance frequency. Since a complex number can be expressed in polar form like:

$$Z = |Z|\left(\cos\theta + j\sin\theta\right) \tag{4.30}$$

With this, the measurements can be compared to Eq. 4.29 as follows:

$$Re(Z) = \frac{R}{(1-\omega^2 LC)^2 + (\omega CR)} = |Z|\cos\theta \tag{4.31}$$

$$Im(Z) = \frac{\omega L(1-\omega^2 LC) - \omega CR^2}{(1-\omega^2 LC)^2 + (\omega CR)} = |Z|\sin\theta \tag{4.32}$$

Nonetheless, this yields an indefinite system of equation with 3 variables R, L and C; but only 2 equations, Eqs. 4.31 and 4.32. A different approach is needed to solve these parameters, and for that reason the finer measurement has been taken. As a rough approximation, the variables in this smaller spectrum are considered constant in the vicinity of the point under study. Therefore, more points can be taken from the spectrum at different frequencies ω_1, ω_2 and ω_3 of which the impedance modulus $|Z_1|$, $|Z_2|$, $|Z_3|$ and the phase angles θ_1, θ_2, θ_3 are all known. In such scenario, 3 equations can be constructed using this information, for instance the real part of the impedance can be converted to:

$$\frac{R}{(1-\omega_1^2 LC)^2 + (\omega_1 CR)} = |Z_1|\cos\theta_1 \tag{4.33}$$

$$\frac{R}{(1-\omega_2^2 LC)^2 + (\omega_2 CR)} = |Z_2|\cos\theta_2 \tag{4.34}$$

$$\frac{R}{(1-\omega_3^2 LC)^2 + (\omega_3 CR)} = |Z_3|\cos\theta_3 \tag{4.35}$$

4.3. Results

The object of this section is to acquire the voltage distribution among the coils using the aforementioned methods, and compare them to draw conclusions for the viability of the model presented. After introducing each result, they are all compared in Subsection 4.3.4.

4.3.1. Experimental Results

Four probes are used during the experiment. The first three are connected as suggested in the diagram from Figure 4.13, measuring the voltage at the motor terminals $V_{terminal}$ (probe 1), at point 1 to ground V_{1-g}(last two coils, probe 2) and point 3 to ground V_{2-g} (last turn, probe 3), while the fourth probe keeps track of the voltage directly supplied by the source, thus using all four channels in the oscilloscope. These four measurements are displayed in Figure 4.18. The results present a close resemblance to experimental data found by R.G. Rhudy et al. [48], as well to L. Guballa et al. [54] and A. Krings et al. [50]; suggesting a relatively decent accuracy of the assumptions taken to build the experimental setup, and a reasonable scalability of the effects to bigger machines than the used in this thesis.

To obtain the voltage drop in each of the coils, some post-processing subtractions are required. For instance, to get the voltage drop in the first coil, the voltage on the last two coils has to be subtracted from the terminal voltage:

$$V_{coil1} = V_{terminal} - V_{1-g} \tag{4.36}$$

$$V_{coil2} = V_{1-g} - V_{2-g} \tag{4.37}$$

$$V_{coil3} = V_{2-g} \tag{4.38}$$

With these calculations Figure 4.21a is drawn to highlight the non-uniformity of the voltage distribution. A voltage overshoot is visible in all the coils, though it is significantly bigger in the first coil. This

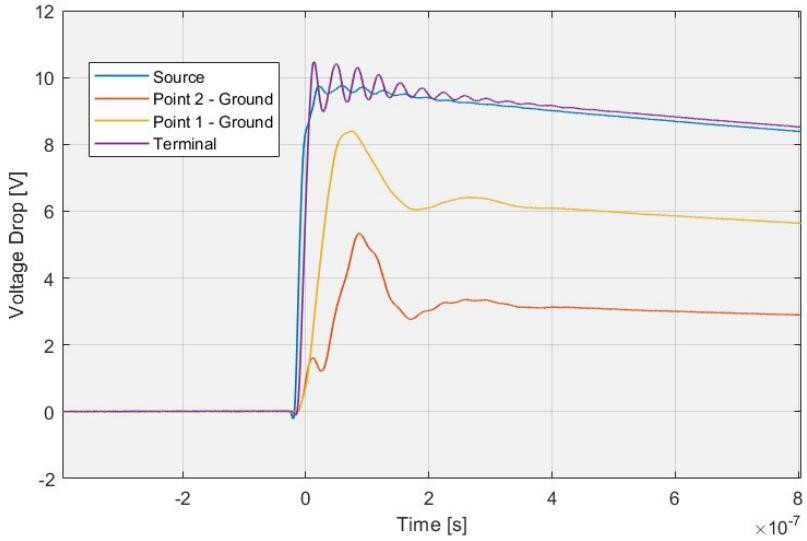

Figure 4.18: Voltage measured with respect to ground in all 3 points described in Figure 4.13, compared to the source voltage.

spike seems to travel along the wiring while losing magnitude, given the small delay seen between its appearance in each coil. After approximately 400 nanoseconds, all of them stabilize into a uniform distribution of the same magnitude, implying the system has a fairly small time constant. This confirms that only the first few nanoseconds after the voltage transient dv/dt are of concern with respects to this effect. Moreover, the results also show another interesting phenomenon: the terminal voltage oscillations corresponding to the Reflected Wave Phenomenon studied in Chapter 3. This is due to the fact that during the manual wiring of the stator core, no attention was put into the length of the extra cable that would connect to the source. In future work, it is recommended to account for both effects during the experimental setup design, in order to more properly tune the influence of each one separately.

4.3.2. Simulation Results: Impedance Analyzer Measurement

The first measurement taken is the capacitance to ground as described in Subsection 4.2.4 by the usage of an LCR meter. To ensure a reliable value, the measurement is taken 4 times independently, and the average value is calculated. This returns a capacitance to ground for all the wiring, the appropriate number for each coil is obtained by simply dividing by 3, assuming all coils are identical.

The rest of the measurements come from the analysis of the spectrums presented in Figures 4.19 and 4.20. These are the full spectrums, used to localize the resonance frequency, after which a finer measurement is taken. The results of this whole analysis (refer to Subsection 4.2.4) is displayed in Table 4.2. Note that this measurements are taken for single coils instead of for all of them combined.

	Coil 1	Coil 2	Coil 3
Resistance	$289.1\ \Omega$	$269.9\ \Omega$	$297.3\ \Omega$
Inductance	$8.5\ \mu\mathrm{H}$	$8.6\ \mu\mathrm{H}$	$8.7\ \mu\mathrm{H}$
Series Capacitance	$3.8\ \mathrm{pF}$	$3.7\ \mathrm{pF}$	$3.8\ \mathrm{pF}$
Ground Capacitance	$29.2\ \mathrm{pF}$	$29.2\ \mathrm{pF}$	$29.2\ \mathrm{pF}$

Table 4.2: Experimentally measured values of RLC per coil. Following the model described in Subsection 4.2.4.

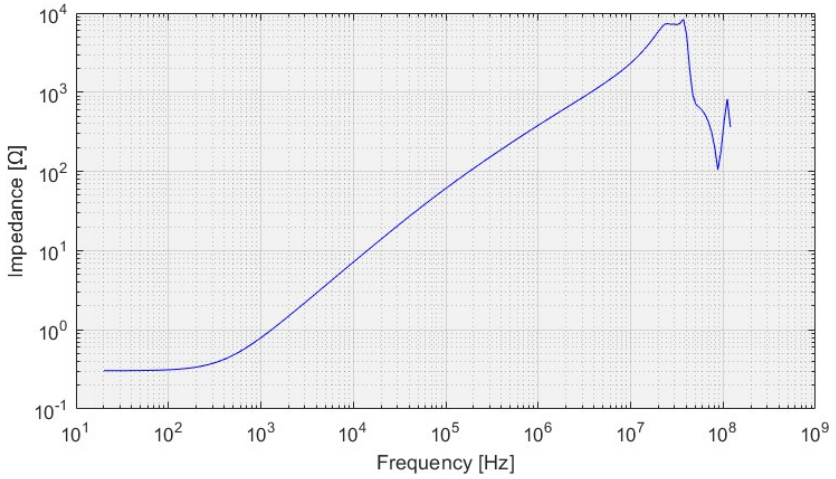

Figure 4.19: Initial impedance spectrum of a single coil, ranging from 20 kHz to over 100 MHz.

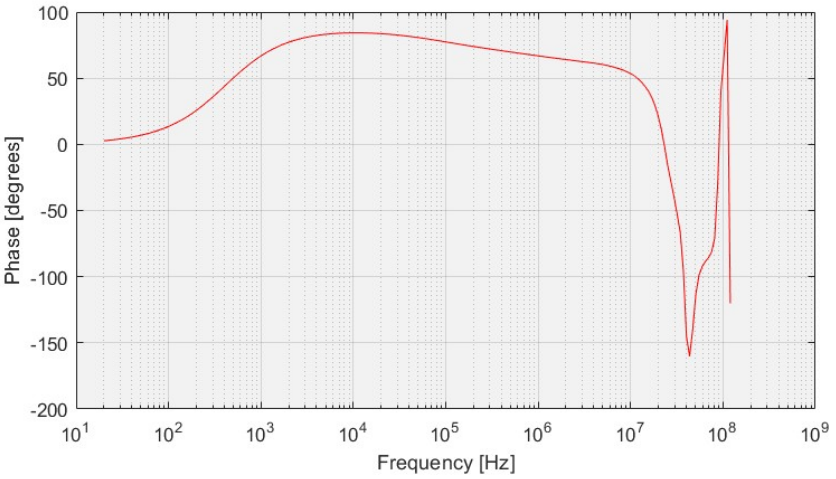

Figure 4.20: Initial phase spectrum of a single coil, ranging from 20 kHz to over 100 MHz.

Some extra measurements were taken at lower frequencies to directly obtain inductance values. This process is done connecting two coils in series and anti-series, repeating the process for every pair of coils possible. By doing this, the mutual inductances can be extracted by considering the inductance of the full bundle of coils i and j to be:

$$L = L_i + L_j - 2M_{ij} \tag{4.39}$$

The values for M_{ij} are not extrapolable to higher frequencies. However, they are useful to notice that, in this geometry, the mutual inductance is two orders of magnitude smaller than the self-inductance. This proportionality is assumed to be relatively conserved and not measured at high frequency. Once these values are introduced into the Simulink model from Figure 4.15, the final voltage distribution per coil is displayed in Figure 4.21b.

4.3.3. Simulation Results: COMSOL

By using the techniques previously discussed in Section 4.2.3, and considering the geometry of the experimental construction, the corresponding RLC parameters of the system are displayed in Table 4.3.

Note that all 3 coils are considered identical, therefore the table shows the parameters corresponding to a single coil.

Magnitude	Value
Resistance	$666.67\ \Omega$
Series Capacitance	$1.07\ \mathrm{pF}$
Ground Capacitance	$30.04\ \mathrm{pF}$
Self-Inductance	$75.07\ \mu\mathrm{H}$
Mutual-Inductance M_{12}	$-2.33\ \mu\mathrm{H}$
Mutual-Inductance M_{23}	$-2.33\ \mu\mathrm{H}$
Mutual-Inductance M_{13}	$-703.53\ \mathrm{nH}$

Table 4.3: Simulated values of RLC parameters per coil using COMSOL Multiphysics.

It is already noticeable that the resistance and inductance values calculated through COMSOL are considerably different than the ones found by measurement with impedance analyzer. It is confirmed by comparison in Figure 4.21c that the calculation through COMSOL is not satisfactory, likely due to the use of the incorrect procedure to compute the inductance, done in a stationary study. This ignores the frequency dependence of such parameter, which is expected to decrease at higher frequencies.

4.3.4. Result Comparison

In this subsection there is a comparative analysis of the results obtained through the different methodologies. As a baseline, the experimental results are considered correct and reliable as inferred in Subsection 4.3.1 from their similarity to literature.

At first sight, it is obvious that the parameters got via COMSOL simulation (Figure 4.21c) are not yielding a satisfactory result. Instead, although the oscillatory behaviour is expected, the dampening of the oscillations is much slower than expected, being roughly two times slower. This is likely due to the unexpectedly high value of inductance computed in COMSOL, which is around 10 times bigger than the values measured with the impedance analyzer, resulting a higher time constant. Despite the flexibility of the software, it was not possible to calculate inductance through a Frequency Domain study, as COMSOL can only do it through the Coil Geometry Analysis study step, which is stationary in nature. Alternatively, some other methods could be explored to approximate the frequency response. For example, a boundary condition could constraint the coil current to the edge of the conductor, simulating the skin depth corresponding to such frequency.

Moreover, the resistance values are also substantially higher. Even though the software seems capable of calculating the effects of the skin and proximity effects (as shown in Figure A.3 in the Appendix), these phenomena are highly dependent of the surrounding medium. The usual value of conductivity for magnetic cores used in these applications are around $2\ \mathrm{MS/m}$. However, this does not account for composite material such as laminated cores, which limit the conductivity in a certain direction. Moreover, it is relevant to recall that the stator was wrapped in a conductive tape to easily ground the whole core. Due to a lack of understanding of these constructions, and a lack of information found in previous studies, assumptions needed to be taken. In this case, the effective conductivity of the stator core is reduced by 10 to account for the lamination.

On the other hand, although the results from the analyzer measurement (Figure 4.21b) are much closer to the experimental data, they are far from perfect as well. Firstly, the magnitude of the overshoots in voltage predicted is far smaller than those of the real case. Two possible causes for this are:

- Miscalculation of the capacitances in COMSOL, due to a faulty geometry. A more proper method for wiring the machine is recommended, such that the distances of each turn to each other and to the core are better controlled.
- The usage of lumped parameter elements, as opposed to distributed parameters, which is more realistic. The finite length of the cable is reflected in the initial response of the coils. Since it takes time for the voltage transient to affect later coils, the total voltage supplied by the source is concentrated in the first one during the first instants of the propagation, as seen in Figure 4.21a.

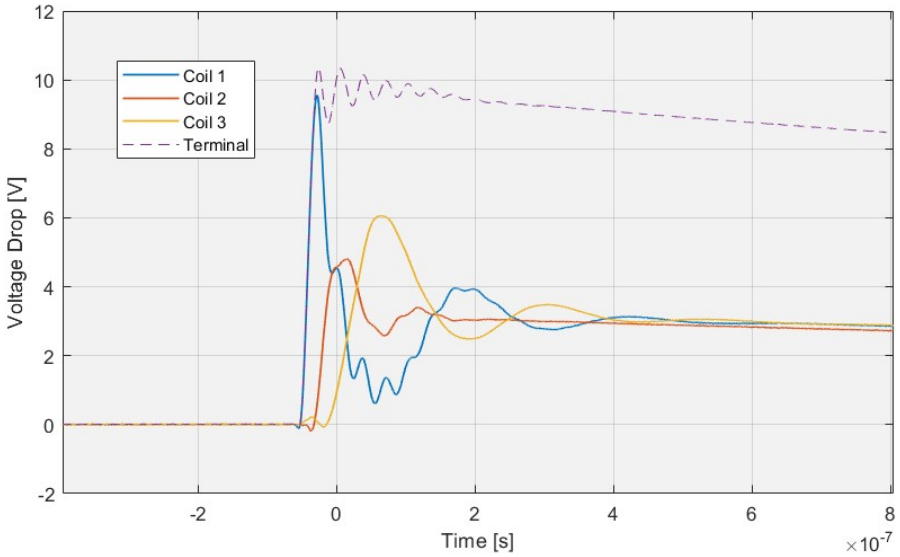

(a) Experimental results.

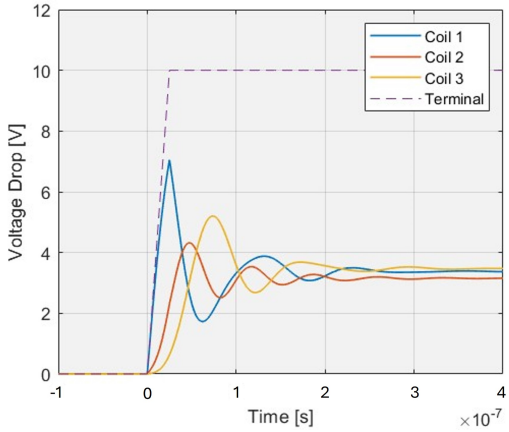

(b) Simulation results using RLC values obtained through measurement with Impedance Analyzer.

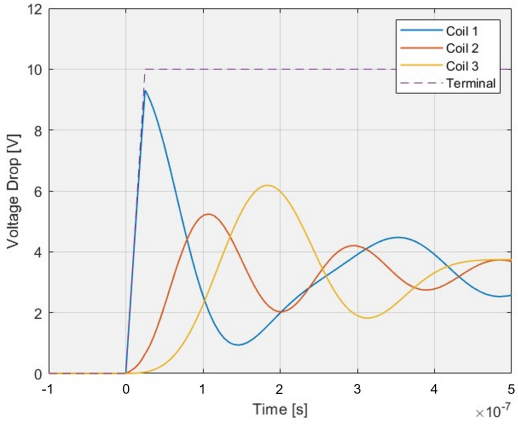

(c) Simulation results using RLC values obtained with COMSOL computation.

Figure 4.21: Voltage distribution among the three coils, with the terminal voltage for reference. Comparison of results acquired through different methods.

Another problem is the time constant, which appears to be too low. This is highlighted by the shorter time delay in between the peaks of each subsequent coil, as well as the shorter dampening time for the whole perturbation. Besides the use of lumped elements as previously stated, another hypothesis might be the cause for the time disagreements: at such high frequencies, the inductor model proposed in Figure 4.14 might not be accurate enough. Some authors such as A. Barzkar and M. Ghassemi [10] propose an alternative model, where the inductance branch of the model is substituted by a frequency dependent 'ladder circuit' (see Figure A.4). While far more complex, it might be necessary to represent the behavior at such frequencies.

Another possibility is the rough assumption of constant RLC values at the vicinity of the resonance point may be too bold, considering the strong frequency dependence around that point. A more statistically-based approach could be more suitable.

4.3.5. Possible Mitigation

Although the reliability of the Simulink model has been proven suboptimal, given the results shown in Subsection 4.3.4, a qualitative sensitivity analysis has been done to test techniques that might mitigate the voltage distribution non-uniformity. The reader is encouraged to review these techniques with a more accurate wiring model.

Of course, a slower rise time does have an effect on the peak voltage of the first coil. Given the same RLC values of the circuit, a slower t_r allows for the voltage pulses to stabilize before they accumulate in the first coil. It could also indirectly reduce the relevance of the capacitance by eliminating faster frequency components. However, this variable also has strong implications towards the effects of RWP, therefore any changes must be done carefully.

Regarding the RLC parameters of the wiring, the resistance mainly controls the dampening of the oscillations, but it does not have much effect on the value of the peaks. The inductance has a big impact in the time constant of the circuit, widening the oscillations. However, it does not affect the peak value to a great extent. The same can be said for the series capacitance. On the other hand, as hypothesised in Subsection 4.2.1, the ground capacitance seems to have a vital role in the maximum value of the voltage peaks in each coil. This is shown is Figure 4.22, where the ground capacitance has been reduced by a factor of 3, to $C_g = 9.7\ \mathrm{pF}$. For reference, the original value measured in the laboratory was $C_g = 29.2\ \mathrm{pF}$ in each coil.

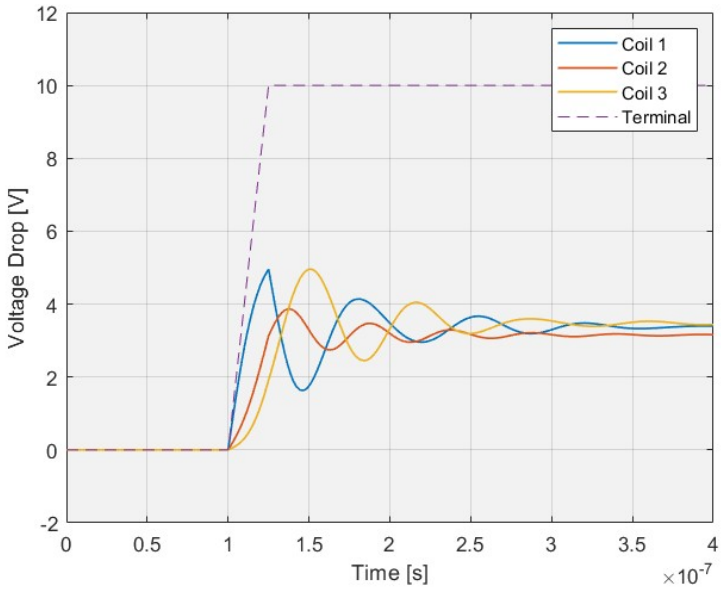

Figure 4.22: Simulation results based on the measured parameters, analog to Figure 4.21b, but with a ground capacitance reduced by a factor of 3.

5

Conclusions & Recommendations

To attain a more sustainable aviation industry, the path of electrification is almost mandatory to avoid the excessive use of fossil fuels. However, such an endeavor does not come without any challenges nor technological barriers. Among other concerns, the reliability of electric machines used in an aircraft is of upmost importance. Besides the obvious safety implications of a motor failure, the industry requires the economical viability of the technology under investment. In order to grant that, electric machines need to have a very long useful lifetime.

The goal of this thesis has been to explore some of the phenomena that may cause a shortening of such lifetime. In particular, the undesired effects branching from the usage of fast switching semiconductor technology for electric motor drives, which can (and often does) cause strong electric stresses in the slot insulation. In this project these effects have been studied in depth in Chapters 3 and 4, laying out a foundation for future work on motor design for aviation.

First, the Reflected Wave Phenomenon RWP was explored in Chapter 3. An extensive literature review was conducted, which explained the appearance of reflections in the feeder cables caused by impedance mismatches between the cable and the motor, using Transmission Line Theory. However, a disagreement between different authors was found in a formula that modeled the overvoltage dependence on the switching rise time and the wire length. This motivated a simulation study to replicated the system, develop a hypothesis and confirm or deny the formulas. Eventually the results showed both formulas to be incorrect, and a new one was proposed to explain the phenomenon. With it, it is possible to adjust the design to mitigate the RWP to a great extent.

Afterwards, the non-uniform voltage distribution was studied in Chapter 4. Supported by previous comparative analyses, the methodology of an equivalent circuit was chosen. However, due to the great variety of different models proposed in literature, it was decided to confirm results experimentally as well. Using the laboratory data, it was observed that the model used can replicate the real case of a motor stator, though not with great accuracy. This chapter is thus considered a step in the right direction, yet not the final benchmark for real life application. Besides the general lack of experience with the softwares and methodologies, some hypothesis for the discrepancies in results are suggested for future work.

5.1. Future Work

All things considered, this project does not put an end to this discussion on electric stress in insulation. On the contrary, it is a baseline for other students to build upon, hence more research is greatly encouraged. This subsection proposes some aspects that require attention to improve the results before applying them to the motor design.

- Address the assumptions taken in the modelling of the inductor. Instead of this simplified circuit, a more appropriate model could be found to represent the behavior in such high frequencies. Among the different models proposed in literature, it is encouraged to test the 'ladder circuit' displayed in Figure A.4 by Barzkar and Ghassemi in [10] and by Sundeep et al. in [51].
- Consider the option of using distributed parameter elements as opposed to the lumped parameters used in this thesis. Although it may bring a very high computational expense, it could also solve some time discrepancies in the Chapter 4 results.
- Even though the results seem accurate enough, the methodology used to calculate the RLC parameters from the impedance analyzer measurements could be improved. In the vicinity of the resonance frequency there is a very fast change of impedance phase angle, meaning the assumption that R, L and C are constant in a small enough range might be suboptimal.
- COMSOL is a very powerful tool that has proven to be extremely accurate if used properly. It is encouraged to explore a correct way to calculate impedance and resistance under high-frequency AC currents, possibly computing a boundary condition for the skin depth.
- It is relevant to note that both phenomena studied in this project do not take place separately in a real motor. After all previous concerns have been addressed, the complete model would include both system, where the resistor used in Chapter 3 is substituted by the whole stator model from Chapter 4. The integration of this complete model is recommended to obtain accurate results.
- Once the full model is built, the resulting voltage overshoots can be utilized as a guideline to design the slot configuration. Originally, an idea was to present a 2D model through COMSOL displaying a heat-map of electrical stress under this voltage distribution.

References

[1] Robin Ramin, Gian Carlo Montanari, and Qichen Yang. “Designing the Insulation System for Motors in Electrified Aircraft: Optimization, Partial Discharge Issues and Use of Advanced Materials”. In: *Materials* 14.24 (2021). Academic Editor: Jianying Li, p. 7555. DOI: 10.3390/ma14247555. URL: https://doi.org/10.3390/ma14247555.

[2] Pablo Alvarez et al. “Review of High Power and High Voltage Electric Motors for Single-Aisle Regional Aircraft”. In: *IEEE Access* 10 (2022). DOI: 10.1109/ACCESS.2022.3215692.

[3] *Bauhaus Luftfahrt - CE-Liner*. Bauhaus Luftfahrt. Accessed 2024. URL: https://www.bauhaus-luftfahrt.net/en/research-areas/hybrid-electric-aviation/ce-liner.

[4] *NASA - N3X*. NASA Glenn Research Center. Accessed 2024. URL: https://www1.grc.nasa.gov/aeronautics/eap/airplane-concepts/n3x/.

[5] *Audi e-tron Battery and Safety*. Audi Technology Portal. AUDI AG. 2021. URL: https://www.audi-technology-portal.com.

[6] Davide D’Amato et al. “Impact of PWM Voltage Waveforms in High-Speed Drives: A Survey on High-Frequency Motor Models and Partial Discharge Phenomenon”. In: *Energies* 15.4 (2022). ISSN: 1996-1073. DOI: 10.3390/en15041406. URL: https://www.mdpi.com/1996-1073/15/4/1406.

[7] Kushan Choksi et al. “Evaluation of Factors Impacting Reflected Wave Phenomenon in WBG Based Motor Drives”. In: *Proceedings of the 2022 International Power Electronics Conference (IPEC-Himeji 2022 -ECCE Asia-)*. Department of Electrical and Computer Engineering, Stony Brook University, Stony Brook, USA. 2022.

[8] Wenzhi Zhou. “Reflected Wave Phenomenon in Inverter-fed Machines with Fast-Switching (high dv/dt) Wide Bandgap Power Converters: Causes, Consequences and Solutions”. PhD thesis. Merchant Venturers Building, Woodland Road, Bristol BS8 1UB, United Kingdom: University of Bristol, June 2022.

[9] Juan Manuel Martínez Tarifa. “Transient Voltage Distribution Along LV Motor Windings Fed with PWM Converters. Insulation Ageing Analysis”. PhD thesis. Leganés (Madrid): Universidad Carlos III of Madrid, Nov. 2005.

[10] Ashkan Barzkar and Mona Ghassemi. “Precise Evaluation of Repetitive Transient Overvoltages in Motor Windings in Wide-Bandgap Drive Systems”. In: *Vehicles* 4.3 (2022), pp. 697–726. DOI: 10.3390/vehicles4030040. URL: https://doi.org/10.3390/vehicles4030040.

[11] Greg C. Stone et al. *Electrical Insulation for Rotating Machines: Design, Evaluation, Aging, Testing, and Repair*. Ed. by Stamatios V. Kartalopoulos. 445 Hoes Lane, Piscataway, NJ 08854: IEEE Press, 2022.

[12] International Electrotechnical Commission. *Rotating Electrical Machines - Part 18-41: Qualification and type tests for Type I electrical insulation systems used in rotating electrical machines fed from voltage converters*. 2019. URL: https://webstore.iec.ch/publication/65356.

[13] International Electrotechnical Commission. *Rotating Electrical Machines - Part 18-42: Qualification and type tests for Type II electrical insulation systems used in rotating electrical machines fed from voltage converters*. 2020. URL: https://webstore.iec.ch/publication/62642.

[14] Han Xiong et al. “Comparison of Effects of Si-Based and SiC-Based Variable Speed Drives on Stator Winding Insulation for Medium-Voltage Propulsion Electric Machines”. In: *ResearchGate* (Apr. 2019). URL: https://www.researchgate.net/publication/335173623.

[15] Juha Pyrhönen, Tapani Jokinen, and Valéria Hrabovcová. *Design of Rotating Electrical Machines*. Second. This edition first published. Chichester, UK: John Wiley & Sons, Ltd, 2014. ISBN: 978-1-118-48794-9.

[16] *Form Wound Insulation*. Accessed 2024. Schulz Group. 2024. URL: https://schulzgroupusa.com/schulznuclear/form-wound.html.

[17] M.K. Hussain and P. Gomez. “Optimal Insulation Design of Form-Wound Stator Winding with Stress Grading System under Fast Rise-Time Excitation”. In: *Electr Eng* 104 (2022), pp. 3853–3865. DOI: 10.1007/s00202-022-01586-5. URL: https://doi.org/10.1007/s00202-022-01586-5.

[18] Saeed Ul Haq. “A Study on Insulation Problems in Drive Fed Medium Voltage Induction Motors”. Doctoral dissertation. Waterloo, Ontario, Canada: University of Waterloo, 2007.

[19] IEEE Standards Coordinating Committee 10, Terms and Definitions. *IEEE Standard Dictionary of Electrical and Electronics Terms (IEEE Standard 100-1996)*. New York, NY, USA, 1996. URL: https://standards.ieee.org/ieee/100/256/.

[20] Michael G. Danikas. “The Definitions Used for Partial Discharge Phenomena”. In: *IEEE Transactions on Electrical Insulation* 28.6 (Dec. 1993). Communication, p. 1075.

[21] L. F. Berzak, S. E. Dorfman, and S. P. Smith. “Paschen’s Law in Air and Noble Gases”. In: (Apr. 2006).

[22] A. A. Martins and M. J. Pinheiro. “On the propulsive force developed by asymmetric capacitors in a vacuum”. In: *Physics Procedia* 20 (2011). Selection and/or peer-review under responsibility of Institute for Advanced studies in Space, Propulsion and Energy Sciences, pp. 112–119. ISSN: 1875-3892. DOI: 10.1016/j.phpro.2011.08.010. URL: https://www.sciencedirect.com/science/article/pii/S1875389211002553.

[23] E. Kuffel, W.S. Zaengl, and J. Kuffel. *High Voltage Engineering: Fundamentals*. Second. Linacre House, Jordan Hill, Oxford OX2 8DP, 225 Wildwood Avenue, Woburn, MA 01801-2041: Newnes, An imprint of Butterworth-Heinemann, 2000.

[24] Alexandre Martins and Mario Pinheiro. “On the propulsive force developed by asymmetric capacitors in a vacuum”. In: *Physics Procedia* 20 (Dec. 2011), pp. 112–119. DOI: 10.1016/j.phpro.2011.08.010.

[25] L. F. Berzak, S. E. Dorfman, and S. P. Smith. *Paschen’s Law in Air and Noble Gases*. Tech. rep. Lawrence Berkeley National Laboratory, Apr. 2006.

[26] Vytenis Babrauskas. “Arc Breakdown in Air over Very Small Gap Distances”. In: Jan. 2013.

[27] S. B. Warder, E. Friedlander, and A. N. Arman. “The influence of rectifier harmonics in a railway system on the dielectric stability of 33-kV cables”. In: *Proceedings of the IEE-Part II: Power Engineering* 98.63 (1951).

[28] Lawrence A. Saunders et al. “Riding the Reflected Wave - IGBT Drive Technology Demands New Motor and Cable Considerations”. In: *IEEE Industry Applications Society Annual Meeting* (1996). Copyright Material IEEE. Paper No. PCIC-96-09.

[29] Peter G. McLaren and Mansour H. Abdel-Rahman. “Modelling of Large AC Motor Coils for Steep-Fronted Surge Studies”. In: *IEEE Transactions on Industry Applications* 24.3 (May 1988).

[30] Erik Persson. “Transient Effects in Application of PWM Inverters to Induction Motors”. In: *IEEE Transactions on Industry Applications* 28.5 (Sept. 1992).

[31] A. von Jouanne, P. Enjeti, and W. Gray. “The Effect of Long Motor Leads on PWM Inverter Fed AC Motor Drive Systems”. In: *IEEE Transactions on Industry Applications* (1995).

[32] Yipu Xu et al. “Impact of High Switching Speed and High Switching Frequency of Wide-Bandgap Motor Drives on Electric Machines”. In: *IEEE Access* 9 (2021). DOI: 10.1109/ACCESS.2021.3086680.

[33] Behrooz Mirafzal, Gary Leonard Skibinski, and Rangarajan Tallam. “A Failure Mode for PWM Inverter-Fed AC Motors Due to the Antiresonance Phenomenon”. In: *IEEE Transactions on Industry Applications* (Nov. 2009). DOI: 10.1109/TIA.2009.2027524.

[34] Gerardus Chr. Paap, Abraham A. Alkema, and Lou van der Sluis. “Overvoltages in Power Transformers Caused by No-Load Switching”. In: *IEEE Transactions on Power Delivery* 10.1 (Jan. 1995).

[35] Balaji Narayanasamy et al. “Reflected Wave Phenomenon in SiC Motor Drives: Consequences, Boundaries, and Mitigation”. In: *IEEE Transactions on Power Electronics* 35.10 (Oct. 2020).

[36] A. von Jouanne, P. Enjeti, and W. Gray. “Application Issues for PWM Adjustable Speed AC Motor Drives”. In: *IEEE Industry Applications Magazine* 5.5 (Sept. 1999).

[37] Annette von Jouanne and Prasad N. Enjeti. “Design Considerations for an Inverter Output Filter to Mitigate the Effects of Long Motor Leads in ASD Applications”. In: *IEEE Transactions on Industry Applications* 33.5 (Sept. 1997).

[38] James L. Kirtley. *Electric Power Principles*. 2nd. Wiley, 2020. Chap. 3. URL: https://ezproxy.torontopubliclibrary.ca/login?url=https://learning.oreilly.com/library/view/-/9781119585176/?ar.

[39] Mark J. Scott et al. “Reflected Wave Phenomenon in Motor Drive Systems Using Wide Bandgap Devices”. In: *IEEE* (2014).

[40] SangCheol Lee and KwangHee Nam. “Overvoltage Suppression Filter Design Methods Based on Voltage Reflection Theory”. In: *IEEE Transactions on Power Electronics* 19.2 (Mar. 2004).

[41] Robert W. Maier and Mark-M. Bakran. “Filterless Mitigation of Machine Terminal Reflected Wave Voltage Stress”. In: *IEEE* (2019).

[42] Jeremy C. G. Wheeler. “Effects of Converter Pulses on the Electrical Insulation in Low and Medium Voltage Motors”. In: *IEEE Electrical Insulation Magazine* (). DEIS Feature Article.

[43] Wenzhi Yuan, Aditya Maheshwari, and Robert W. Maier. “Optimal Time-Domain Pulse Width Modulation for Three-Phase Inverters”. In: *Electrical and Computer Engineering, University of Maryland* (2019). ResearchGate. URL: https://www.researchgate.net/publication/332977818_Optimal_Time-Domain_Pulse_Width_Modulation_for_Three-Phase_Inverters.

[44] Tennessee Tech University. *Chapter 4 Model of 3-phase Inverter*. Online. URL: https://www.tntech.edu/engineering/pdf/cesr/ojo/asuri/Chapter4.pdf.

[45] Aditya Shekhar. *Electronic Power Conversion ET4119 / SET3095, Unit 9 & 10*. Lecture slides taken from TU Delft Brightspace, student login account required. Lectures are available for free in: https://www.youtube.com/@NewMediaCentre. 2022. URL: https://brightspace.tudelft.nl/d2l/le/content/501109/viewContent/3049393/View.

[46] Ned Mohan, Tore M. Undeland, and William P. Robbins. *Power Electronics: Converters, Applications, and Design*. 2nd. New York, Chichester, Brisbane, Toronto, Singapore: John Wiley & Sons, Inc., 1995.

[47] G. Lupo et al. “Multiconductor transmission line analysis of steep-front surges in machine windings”. In: *Dielectrics and Electrical Insulation, IEEE Transactions on* 9 (July 2002), pp. 467–478. DOI: 10.1109/TDEI.2002.1007711.

[48] R.G. Rhudy, E.L. Owen, and D.K. Sharma. “Voltage Distribution Among the Coils and Turns of a Form Wound AC Rotating Machine Exposed to Impulse Voltage”. In: *IEEE Transactions on Energy Conversion* EC-1.2 (June 1986), pp. 39–44.

[49] Behrooz Mirafzal et al. “Universal Induction Motor Model With Low-to-High Frequency-Response Characteristics”. In: *IEEE Transactions on Industry Applications* 43.5 (Sept. 2007), pp. 1207–1216.

[50] Andreas Krings et al. “Experimental Investigation of the Voltage Distribution in Form Wound Windings of Large AC Machines”. In: Sept. 2016. DOI: 10.1109/ICELMACH.2016.7732753.

[51] Shubham Sundeep, Jiabin Wang, and Antonio Griffo. “Holistic Modeling of High-Frequency Behavior of Inverter-Fed Machine Winding, Considering Mutual Couplings in Time Domain”. In: *IEEE Transactions on Industry Applications* 57.6 (Nov. 2021), pp. 5712–5721.

[52] Marjan Popov et al. “Computation of Very Fast Transient Overvoltages in Transformer Windings”. In: *IEEE Transactions on Power Delivery* 18.4 (Oct. 2003), pp. 1268–1274.

[53] Sara Mahdavi and Kay Hameyer. “High Frequency Equivalent Circuit Model of the Stator Winding in Electrical Machines”. In: *IEEE Xplore*. ©2012 IEEE. IEEE. 2012. ISBN: 978-1-4673-0142-8.

[54] L. Gubbala et al. “Voltage distribution in the windings of an AC motor subjected to high dV/dt PWM voltages”. In: *Proceedings of PESC ’95 - Power Electronics Specialist Conference*. Vol. 1. 1995, 579–585 vol.1. DOI: 10.1109/PESC.1995.474867.

[55] G. Grandi et al. “Stray capacitances of single-layer air-core inductors for high-frequency applications”. In: *IAS ’96. Conference Record of the 1996 IEEE Industry Applications Conference Thirty-First IAS Annual Meeting*. Vol. 3. 1996, 1384–1388 vol.3. DOI: 10.1109/IAS.1996.559246.

[56] E. Di Lorenzo. *The Maxwell Capacitance Matrix*. White Paper WP110301. Copyright 2020 E. Di Lorenzo. FastFieldSolvers S.R.L., June 2020.

[57] Clayton R. Paul and Arthur E. Feather. “Computation of the Transmission Line Inductance and Capacitance Matrices from the Generalized Capacitance Matrix”. In: *IEEE Transactions on Electromagnetic Compatibility* EMC-18.4 (1976), pp. 175–183. DOI: 10.1109/TEMC.1976.303498.

[58] B.S. Oyegoke. “Indirect boundary integral equation method as applied for wave propagation in the stator winding of an electric machine”. English. In: *IEE Proceedings - Science, Measurement and Technology* 144 (5 Sept. 1997), 223–227(4). ISSN: 1350-2344. URL: https://digital-library.theiet.org/content/journals/10.1049/ip-smt_19971427.

[59] Jose Enrique Ruiz Sarrió, Claudia Martis, and Fabien Chauvicourt. “Numerical Computation of Parasitic Slot Capacitances in Electrical Machines”. In: *2020 International Conference and Exposition on Electrical And Power Engineering (EPE)*. 2020, pp. 146–150. DOI: 10.1109/EPE50722.2020.9305616.

[60] Clayton R. Paul and Arthur E. Feather. “Computation of the Transmission Line Inductance and Capacitance Matrices from the Generalized Capacitance Matrix”. In: *IEEE Transactions on Electromagnetic Compatibility* EMC-18.4 (1976), pp. 175–183. DOI: 10.1109/TEMC.1976.303498.

[61] J.R. Mautz, R.F. Harrington, and C.G. Hsu. “The inductance matrix of a multiconductor transmission line in multiple magnetic media”. In: *IEEE Transactions on Microwave Theory and Techniques* 36.8 (1988), pp. 1293–1295. DOI: 10.1109/22.3673.

[62] Alan Payne. “SKIN EFFECT, PROXIMITY EFFECT AND THE RESISTANCE OF CIRCULAR AND RECTANGULAR CONDUCTORS”. In: (May 2021).

[63] B.S. Oyegoke. “A comparative analysis of methods for calculating the transient voltage distribution within the stator winding of an electric machine subjected to steep-fronted surge”. In: *1997 Eighth International Conference on Electrical Machines and Drives (Conf. Publ. No. 444)*. 1997, pp. 294–298. DOI: 10.1049/cp:19971086.

[64] United States Environmental Protection Agency. *Electromagnetic Signal Attenuation (Skin Depth)*. Accessed: 2024. 2024. URL: https://www.epa.gov/environmental-geophysics/electromagnetic-signal-attenuation-skin-depth#:~:text=Skin%20depth%20is%20the%20depth,EM%20wave%20is%20propagating%20through.

[65] H.A. Wheeler. “Formulas for the Skin Effect”. In: *Proceedings of the IRE* 30.9 (1942), pp. 412–424. DOI: 10.1109/JRPROC.1942.232015.

[66] Miroslav A Prša, Karolina K Kasaš-Lažetić, and Nikola D Mučalica. “Skin effect and proximity effect in a real, high voltage, double three-phase system”. In: *2011 IEEE EUROCON - International Conference on Computer as a Tool*. 2011, pp. 1–4. DOI: 10.1109/EUROCON.2011.5929245.

[67] RS PRO. *RS PRO 357-744 Datasheet*. Accessed: 2024. 2024. URL: https://docs.rs-online.com/a66d/0900766b8157f395.pdf.

[68] Gabriele Grandi et al. “Model of Laminated Iron-Core Inductors for High Frequencies”. In: *Magnetics, IEEE Transactions on* 40 (Aug. 2004), pp. 1839–1845. DOI: 10.1109/TMAG.2004.830508.

A

Appendix A: Parameter Calculation

$$\begin{bmatrix} 7.44 & 6.38 & 0 & 0 & 0 & 0 \\ 6.38 & 3.19 & 6.38 & 0 & 0 & 0 \\ 0 & 6.38 & 3.19 & 6.38 & 0 & 0 \\ 0 & 0 & 6.38 & 3.19 & 6.38 & 0 \\ 0 & 0 & 0 & 6.38 & 3.19 & 6.38 \\ 0 & 0 & 0 & 0 & 6.38 & 7.44 \end{bmatrix} \times 10^{-10} F \tag{A.1}$$

$$\begin{bmatrix} 8.31 \times 10^{-10} & 6.44 \times 10^{-10} & 1.72 \times 10^{-16} & 9.56 \times 10^{-22} & 5.26 \times 10^{-27} & 2.93 \times 10^{-32} \\ 6.44 \times 10^{-10} & 3.92 \times 10^{-10} & 6.44 \times 10^{-10} & 1.73 \times 10^{-16} & 9.49 \times 10^{-22} & 5.28 \times 10^{-27} \\ 1.72 \times 10^{-16} & 6.44 \times 10^{-10} & 3.93 \times 10^{-10} & 6.44 \times 10^{-10} & 1.71 \times 10^{-16} & 9.53 \times 10^{-22} \\ 9.53 \times 10^{-22} & 1.72 \times 10^{-16} & 6.44 \times 10^{-10} & 3.93 \times 10^{-10} & 6.44 \times 10^{-10} & 1.72 \times 10^{-16} \\ 5.28 \times 10^{-27} & 9.50 \times 10^{-22} & 1.73 \times 10^{-16} & 6.44 \times 10^{-10} & 3.92 \times 10^{-10} & 6.44 \times 10^{-10} \\ 2.92 \times 10^{-32} & 5.27 \times 10^{-27} & 9.56 \times 10^{-22} & 1.72 \times 10^{-10} & 6.43 \times 10^{-10} & 8.31 \times 10^{-10} \end{bmatrix} F \tag{A.2}$$

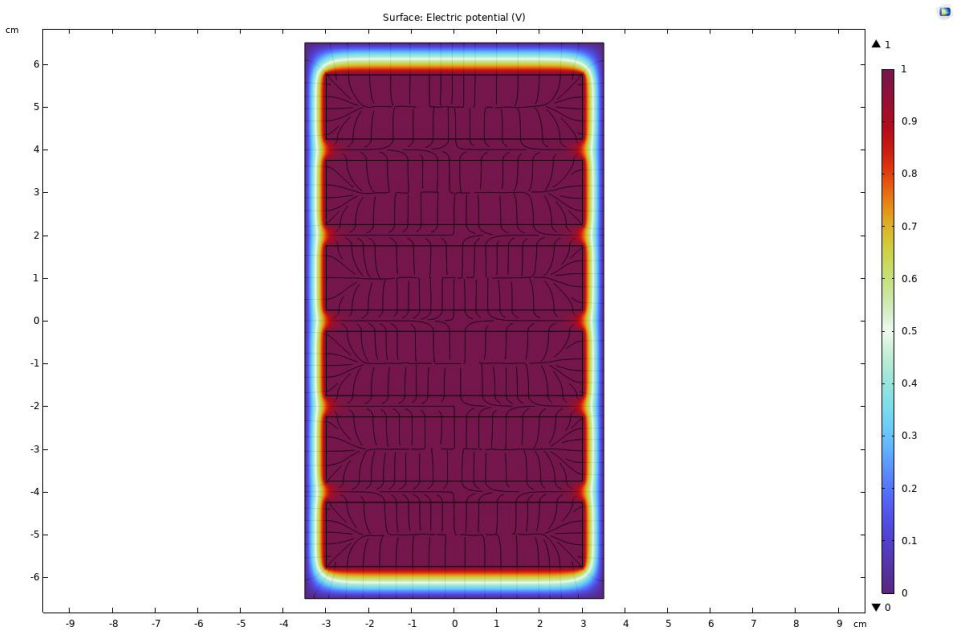

Figure A.1: Electric potential of a generic model, when all conductors are at $1V$. This is used to calculate capacitances to ground.

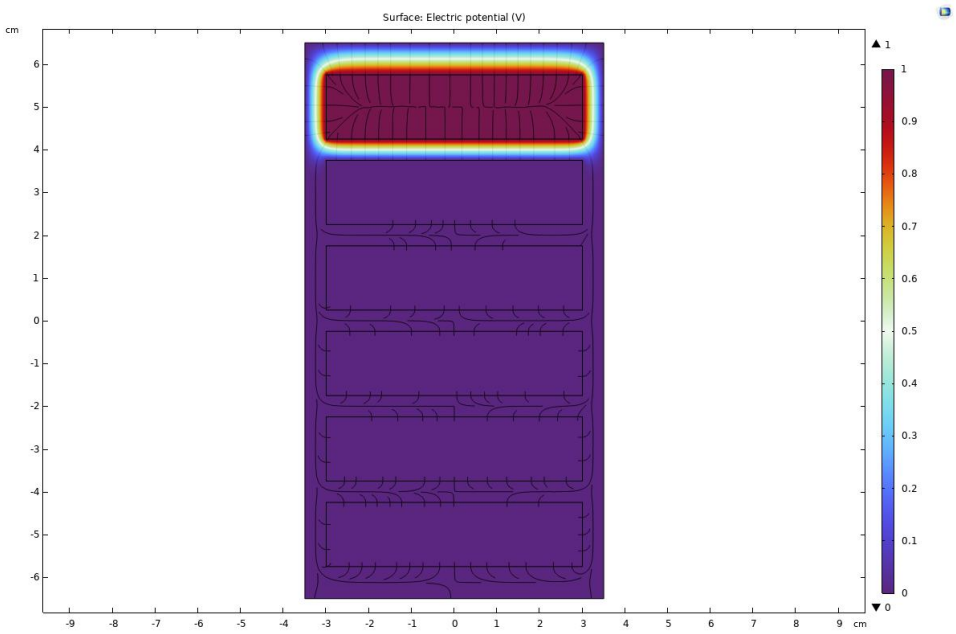

Figure A.2: Electric potential of a generic model, when one conductors is at $1V$ while all others are kept at 0. This is used to calculate mutual turn-to-turn capacitances.

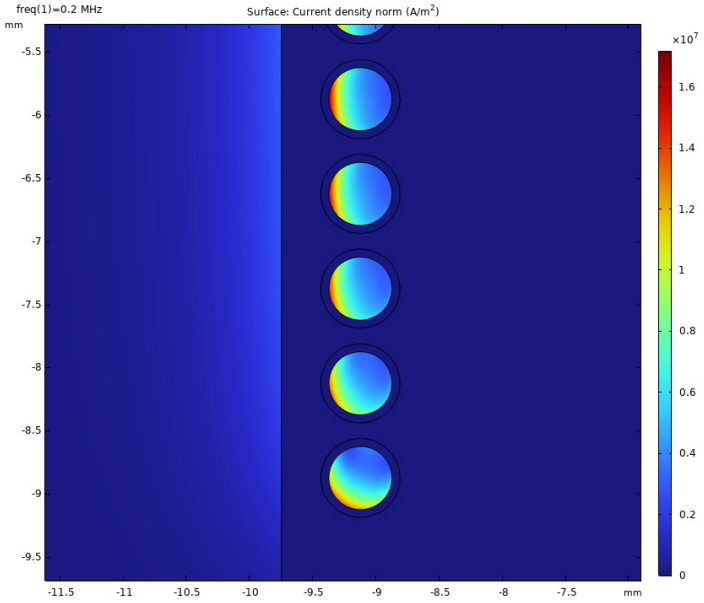

Figure A.3: Cross section representation of the current density through the cable at different positions within the coil. Some eddy currents are visible in the core, although the real stator is laminated to prevent these. Unexpectedly, in this simulation the current flows mostly at the left part of the copper, closer to the core; likely due to faulty modelling.

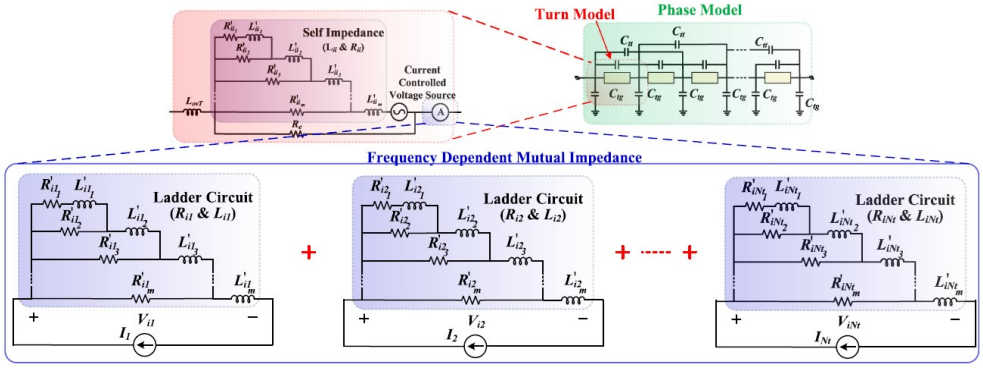

Figure A.4: Frequency-dependent ladder circuit representation of the phase winding proposed by S. Sundeep et al. [51]

B

Appendix B: Filter Design

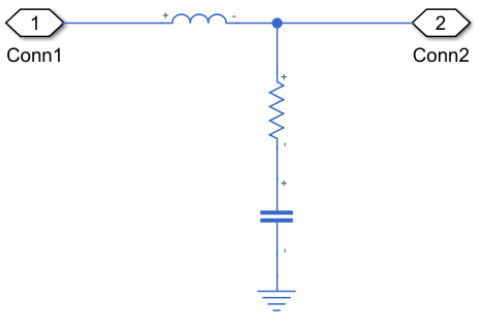

Figure B.1: RLC dv/dt filter model used at the inverter side.

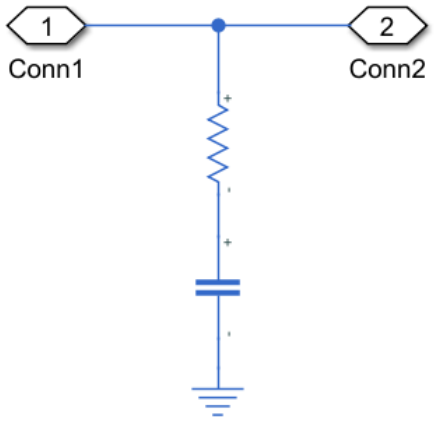

Figure B.2: RC filter model used at the terminal side.

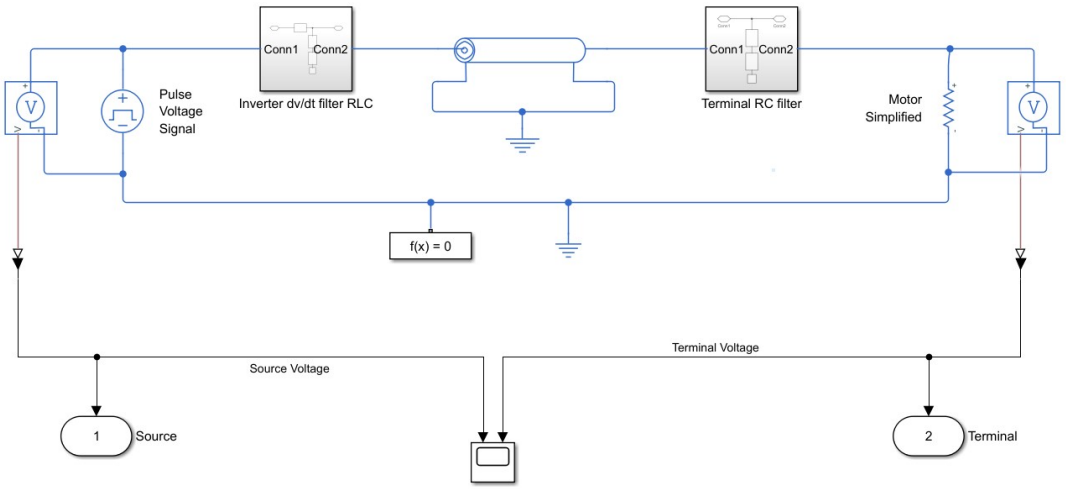

Figure B.3: Transmission Line model with corresponding voltage filters.

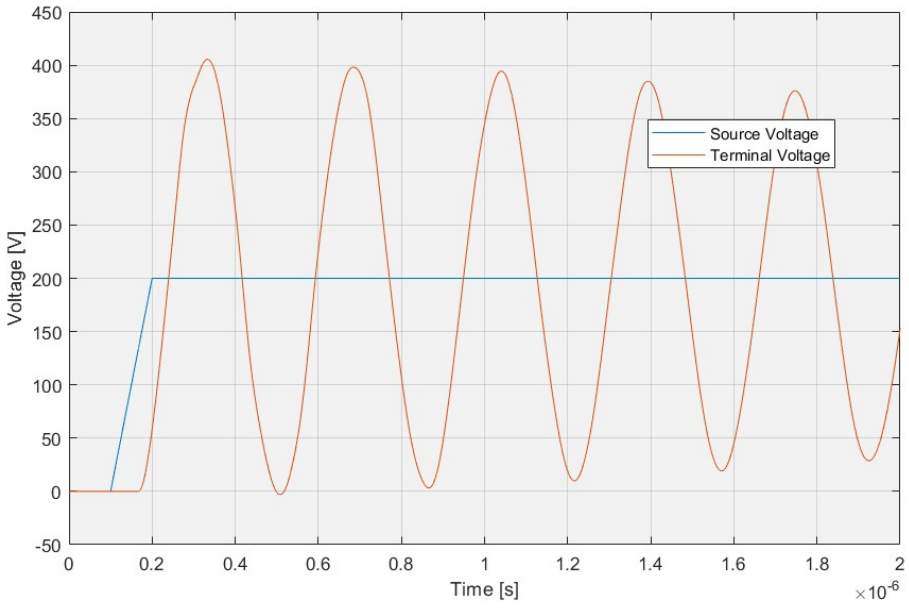

Figure B.4: RWP voltage response when using only the RLC filter at the inverter side.

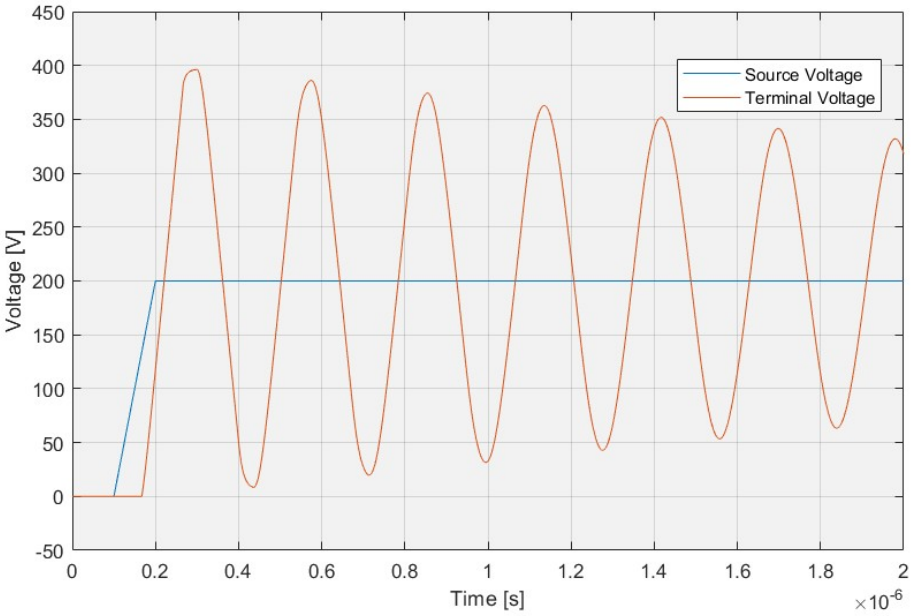

Figure B.5: RWP voltage response when using only the RC filter at the terminal side.

RLC dv/dt filter, inverter side	
R	$190\ \Omega$
L	$0.2\ \mu\mathrm{H}$
C	$75\ \mathrm{pF}$

RC filter, terminal side	
R	$65\ \Omega$
C	$75\ \mathrm{pF}$

Table B.1: Parameters used in the filters implemented. Based on [37].